Research Square

Preprints are preliminary reports that have not undergone peer review.
They should not be considered conclusive, used to inform clinical practice,
or referenced by the media as validated information.

Ultrasonic servoing for autonomous intraoperative robotic imaging in neurosurgery: ex-vivo experiments and medical assessment

Michael Dyck

michael.dyck@dlr.de

Deutsches Zentrum für Luft- und Raumfahrt e. V. (DLR)

Arne Sachtler

Technical University of Munich

Luke Dixon

Imperial College Healthcare NHS Trust

Alexander Kirst

Deutsches Zentrum für Luft- und Raumfahrt e. V. (DLR)

Bernhard Weber

Deutsches Zentrum für Luft- und Raumfahrt e. V. (DLR)

Alistair Weld

Imperial College London

Sophie Camp

Imperial College Healthcare NHS Trust

Stamatia Giannarou

Imperial College London

Alexander Dietrich

Deutsches Zentrum für Luft- und Raumfahrt e. V. (DLR)

Julian Klodmann

Deutsches Zentrum für Luft- und Raumfahrt e. V. (DLR)

Alin Albu-Schäffer

Deutsches Zentrum für Luft- und Raumfahrt e. V. (DLR)

Article

Keywords:

Posted Date: November 24th, 2026

DOI: https://doi.org/10.21203/rs.3.rs-11502601/v1

License: This work is licensed under a Creative Commons Attribution 4.0 International License.
Read Full License

Additional Declarations: Competing interest reported. The following patent applications related to this work have been filed: German patent application 2025062123450627DE, international patent application PCT/EP2026/068315 (M.D., A.S., J.K., A.A.-S.).

Ultrasonic servoing for autonomous intraoperative robotic imaging in neurosurgery: ex-vivo experiments and medical assessment

Michael Dyck[1,2*], Arne Sachtler[2,1], Luke Dixon[3], Alexander Kirst[1], Bernhard Weber[1], Alistair Weld[4], Sophie Camp[5], Stamatia Giannarou[4,6], Alexander Dietrich[1], Julian Klodmann[1=], and Alin Albu-Schäffer[1,2=]

[*]Corresponding author. Email: michael.dyck@dlr.de

[1]German Aerospace Center (DLR), Institute of Robotics and Mechatronics, 82234 Wessling, Germany.

[2]Technical University of Munich, Department of Computer Engineering, 85748 Garching, Germany.

[3]Imperial College London, Faculty of Medicine, Division of Surgery and Cancer, and Imperial College Healthcare NHS Trust, Department of Neuroradiology, London, UK.

[4]Imperial College London, The Hamlyn Centre, London SW7 2AZ, UK.

[5]Imperial College London, Faculty of Medicine, Division of Surgery and Cancer, and Imperial College Healthcare NHS Trust, Department of Neurosurgery, London, UK.

[6]Imperial College London, Faculty of Medicine, Department of Surgery and Cancer, London SW7 2AZ, UK.

[=]These authors contributed equally.

Abstract

Intraoperative ultrasound is a valuable tool for guiding brain tumor resection, yet its clinical utility is limited by the expertise required to acquire high-quality images and the resulting operator variability. While robotic ultrasound systems exist for many applications, autonomous scanning of the brain remains unsolved due to the tissue's exceptional softness and stringent safety requirements. Here we propose *ultrasonic servoing*, which uses real-time acoustic-coupling detection from the ultrasound image together with surface-centric impedance control to achieve stable coupling and perpendicular probe alignment on ex-vivo porcine brain tissue without preoperative mapping or external sensing. In a single-blind assessment by eight neurosurgeons and radiologists, robotically acquired scans were found to have comparable or even superior image quality to those acquired by an expert sonographer, while the system maintained minimal interaction forces and higher inter-scan reproducibility compared to manual scanning. By eliminating operator variability and ensuring safe tissue interaction, this work demonstrates that autonomous robots can assist with standardized, expert-level intraoperative imaging, offering a path toward more accessible and reliable intraoperative ultrasound imaging in neurosurgical oncology.

One-Sentence Summary

Ultrasonic servoing enables standardized, expert-quality intraoperative robotic ultrasound imaging of delicate brain tissue in neurosurgical oncology.

INTRODUCTION

CANCER poses a major global health challenge [1]. Among all types, brain cancer has the highest average years of life lost [2]. Maximal safe resection, i.e., the removal of as much tumor tissue as safely possible, is the main treatment option for most primary brain tumors and a crucial aspect of contemporary neuro-oncology treatment [3]. Studies show the importance of maximal safe resection in overall and progression-free survival and quality of life [4–6].

During surgery, intraoperative brain shift and soft-tissue deformation can cause a spatial misalignment of $5\text{-}15\ \mathrm{mm}$ between preoperative images and intraoperative anatomy [7]. This limits the reliability of preoperative images for real-time surgical guidance. Accurately delineating brain tumor from normal brain becomes difficult, potentially resulting in inadvertent damage or incomplete tumor removal [4, 5, 7]. Consequently, real-time intraoperative imaging becomes beneficial. Ultrasound as a medical imaging modality provides non-invasive and radiation-free real-time images with a relatively small footprint [8]. Its use during surgery (intraoperative ultrasound) has proven vital to detect and diagnose brain pathologies [9, 10]. Evidence consistently demonstrates that intraoperative ultrasound increases gross total resection rates by $15\text{-}25\ \%$ and correlates with improved progression-free survival [11].

Over the last three decades, ultrasound has matured as a tool for intraoperative neurosurgical imaging, and has been adopted into routine clinical practice in numerous neurosurgical centers [10–17]. However, it lacks standardization and suffers from high inter-operator and inter-institutional variability. Acquiring high-quality images poses a distinct visuo-tactile challenge, requiring extensive training and experience to achieve consistent results [18]. These challenges hinder the widespread adoption of intraoperative ultrasound in neuro-oncology [9]. To mitigate the limitations of manual ultrasound, robotic ultrasound systems (RUSS) have been proposed to standardize acquisition and support experts in performing reproducible, target-specific imaging [19, 20]. The vast majority of autonomous RUSS research focuses on extracorporeal ultrasound scanning at the skin surface, primarily applied to abdominal, cardiovascular, obstetric, spine, or breast diagnosis [19–23]. However, intraoperative organ tissue scanning presents a distinct set of challenges. While commonly applied to the scanning of soft organs during liver, pancreas or kidney surgery [24], brain tissue represents a particular extreme in terms of compliance. It is exceptionally soft, with an elastic modulus of only about $1\ \mathrm{kPa}$, and thus significantly lower than that of liver tissue ($\approx 10\ \mathrm{kPa}$) and roughly two orders of magnitude lower than that of skin [25], making it highly susceptible to large deformation under minimal stress. This makes it essential to perform safe and gentle ultrasound scanning to avoid tissue damage, posing challenges not present in other applications.

Controllers for RUSS mainly follow a hybrid force/position scheme, controlling the force along the probe's longitudinal axis for acoustic coupling and motion tangential to the tissue, typically combining

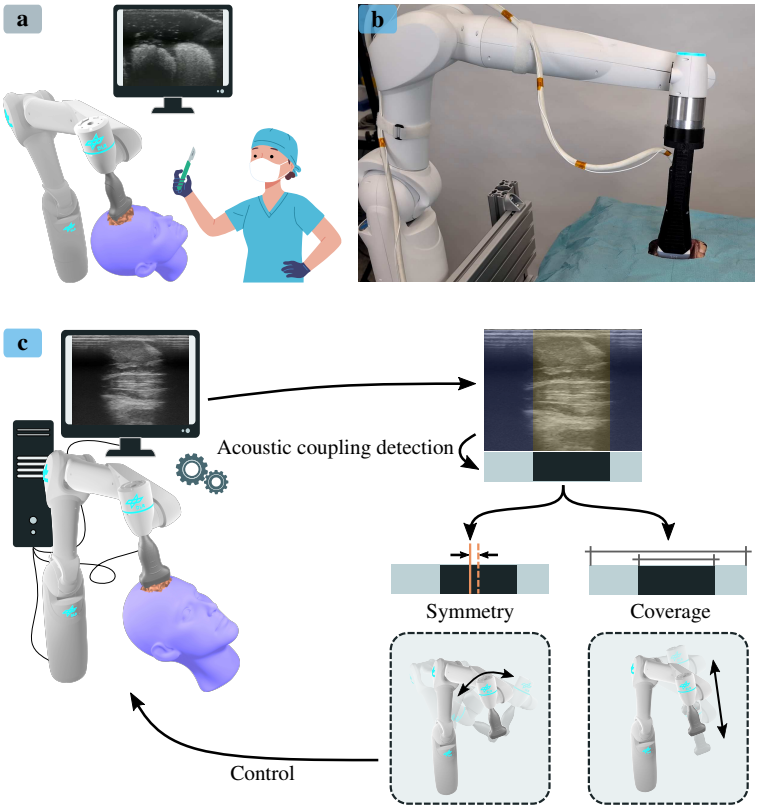

Fig. 1. **Robotic ultrasound brain tissue scanning.** (**a**) Intraoperative robotic scanning for brain tumor resection guidance in neurosurgical oncology. (**b**) Robotic scanning setup on ex-vivo porcine brain. (**c**) Ultrasonic servoing control: The robot adapts position and orientation of the ultrasound probe based on acoustic coupling detection in the ultrasound image.

feed-forward force control with Cartesian impedance [26, 27]. Cartesian impedance control alone can realize probe-tissue coupling by continuously offsetting desired position against the tissue surface [28].

Perpendicular alignment is critical to avoid signal loss from specular reflection. Several systems rely on external sensors, such as RGB-D cameras that capture the tissue surface, or load cells [29] or optical tracking [30] to measure the probe's orientation relative to the surface.

Other methods control the probe pose from the ultrasound image itself, quantifying image quality with confidence maps [31] to optimize acquisition [32–34]. One such approach additionally combines image feedback with a dedicated force/torque sensor to achieve perpendicularity [35].

Each of these strategies, however, encounters specific obstacles when scanning brain tissue. First, neurosurgery demands very low interaction forces, where force measurements become unreliable due to sensor sensitivity and noise, making it difficult to maintain stable coupling and alignment. Further, applying standard stiffness settings to parameterize an impedance controller can lead to excessive force or conversely loss of acoustic coupling. Second, force measurement alone does not quantify acoustic coupling, and thus image quality. Third, in the complex environment of a craniotomy, where a clear view of the brain tissue surface is already rare, external tracking becomes difficult due to optical markers frequently being obstructed by surgical instruments or fluids. Moreover, additional hardware increases the footprint and requires preoperative calibration. Finally, standard image-quality confidence maps struggle with the brain's anatomy, whose naturally hypoechoic structures (ventricles, fluid-filled cavities) may be misinterpreted as poor-quality image or noise [36], potentially leading to unwanted control behavior. These limitations motivate a self-contained coupling and alignment method based on ultrasound image feedback, that can be used without or in combination with external sensing.

Our approach

We propose *ultrasonic servoing*, a paradigm shift in robotic ultrasound control: we adapt and enhance the promising concept of *acoustic coupling detection* per image column based on acoustic shadow patterns presented in [36] to achieve real-time quantification of probe-tissue coupling. Using this probe-tissue coupling to estimate the tissue surface geometry at the point of probe-tissue contact, we establish a synergistic link to the *surface-centric impedance control* framework [37] that allows operational space control relative to the geometry of curved surfaces. These principles are integrated into a closed-loop control system capable of autonomous, gentle interaction with delicate brain tissue while implicitly maintaining minimal interaction forces. Our prior work [38] demonstrated the feasibility of robotic intraoperative ultrasound on soft-tissue phantoms, relying on external RGB-D cameras and ArUco markers for surface reconstruction. The present work advances beyond that in three fundamental aspects: (1) the control paradigm shifts from externally-sensed surface geometry, eliminating the need for external cameras, fiducial markers, and preoperative mapping: instead, purely ultrasound-image-feedback-based ultrasonic servoing uses an Unscented Kalman Filter (UKF) to estimate the unknown tissue surface geometry online; (2) experiments move from gelatin phantoms to real ex-vivo porcine brain tissue; and (3) validation moves from a single preliminary landing test to a multi-institutional, single-blind clinical assessment against expert manual scanning.

The proposed approach is illustrated in Fig. 1, which shows the application of robotic intraoperative ultrasound in brain surgery (Fig. 1a) and provides an overview of the robotic ultrasound control method (Fig. 1b,c). *Ultrasonic servoing* is implemented by a visual servoing control loop based purely on ultrasound image feedback with two objectives: (1) achieving perpendicular probe orientation to prevent signal loss from specular reflection by exploiting a *symmetry* criterion, and (2) adjusting penetration depth to realize a desired probe-tissue coupling without contact-related image artifacts in terms of a *coverage* criterion. The tissue surface geometry is estimated simultaneously via an *Unscented Kalman Filter* for local surface reconstruction.

We present a complete demonstration of autonomous robotic ultrasound imaging on ex-vivo porcine brain tissue with verified clinical image quality based on expert clinical assessment. To ensure clinical applicability, we define three fundamental operational criteria:

- **Stable coupling:** Preservation of consistent acoustic coupling without loss of contact or loss of perpendicular alignment. Acoustic coupling is calculated from the ultrasound image as binary classification of image columns into coupling or no coupling. From this, two metrics can be extracted (cf. Fig. 1c):
  - **Coverage (c)** The ratio of acoustic coupling area to the total image width ($c \in [0, 1]$). High coverage minimizes acoustic shadow artifacts.
  - **Symmetry (s)** The spatial distribution of contact relative to the probe's center column ($s \in [-1, 1]$). Symmetry ($s \approx 0$) indicates perpendicular in-plane probe alignment.
- **Safe scanning:** Realization and preservation of a certain coverage c_{des}, without exerting large forces. Given the soft, delicate nature of brain tissue, this is essential to minimize tissue deformation and prevent damage.
- **Reproducibility:** Ability to consistently replicate a predefined scanning protocol across repeated acquisitions. This is quantified by the statistical consistency of coverage (c) and symmetry (s), probe motions and tissue interaction. High reproducibility ensures standardization and reliable intraoperative imaging.

Our work establishes the feasibility of robotic assistance in neurosurgical oncology. We demonstrate that our autonomous robotic system can satisfy the dual requirements of patient safety and high image quality.

RESULTS

Experiments to demonstrate our proposed ultrasonic servoing control follow a standardized scanning protocol [9] comprising coronal and sagittal fan motions (Fig. 2b). The reference coordinate system at the tip of the ultrasound probe is introduced in Fig. 2a. Note that medical terms for rotational probe motions (fan, rock, rotate) can be directly mapped to the corresponding robotics notations (roll, pitch, yaw) and will be used interchangeably. The scanning protocol consists of one fan motion in coronal and sagittal plane, respectively. A rotation by 90° about the probe's longitudinal axis connects these two fan motions. Manual scans following this protocol by co-author Luke Dixon[1] serve as the expert reference. All robotic scans stand in comparison to this manual acquisition. Experiments were conducted on two ex-vivo porcine heads, with five trials per head and method of acquisition, yielding five manual and four robotic scans per head. Two robotic scans were interrupted due to workspace limit issues and thus excluded from the evaluation. Both heads were continuously cooled in an ice bath and the acquisition order was counterbalanced across the two heads.

In total, ten manual ($N_m = 10$) and eight complete robotic ($N_r = 8$) scans were recorded. All plots that visualize results of one experimental trial, rather than showing statistics, are taken from one and the same specific individual scan. Further, data is cut along the time dimension to start at $t = 0$ s, which is set to the instant of first contact between ultrasound probe and tissue.

Safe scanning and stable coupling on brain tissue

Ultrasonic servoing extracts two quantities from the real-time ultrasound image (Fig. 1c): coverage c, the fraction of the image with acoustic coupling, and symmetry s, the offset of that coupling from the image's center column. The control objective is then (1) to realize a desired, operator-specified coverage c_{des} and (2) to maintain that coverage symmetrically ($s_{\text{des}} = 0$): the former via motion along the probe's longitudinal axis, the latter via the probe's in-plane orientation. As visualized in Fig. 3a, the desired coverage is achieved by spanning a virtual spring between desired and actual probe position, generating passive interaction forces. In other words, the robot pushes the probe onto the tissue only as much as necessary to maintain stable acoustic coupling, implicitly keeping interaction forces minimal.

Fig. 2d,f demonstrates the successful autonomous robotic execution of the scanning protocol on ex-vivo brain tissue, showing contact establishment, an automatic probe-alignment routine (a 90° yaw rotation and back), and execution of the prescribed scanning protocol. The corresponding manual execution can be seen in Fig. 2c,e. The probe translation, shown relative to the instant of contact establishment in Fig. 2g,h, is larger for the expert sonographer (≈ 143 mm), who combines the fan motions with translation to reach below and beyond the craniotomy borders. Such a more complex motion was not implemented as part of the robotic scanning protocol (total translation ≈ 35 mm).

Coverage remained stable throughout the robotic scan ($c_r = 0.86 \pm 0.14$, $c_{\text{des}} = 0.9$) vs. $c_m = 0.65 \pm 0.22$ for the manual scan, indicating more stable and consistent probe-tissue coupling during robotic acquisition (Fig. 3b,c). Interaction forces (Fig. 3d,e) were lower for the robotic ($|F_r| = 0.50 \pm 0.37$ N) than for the manual scan ($|F_m| = 0.76 \pm 0.53$ N), with maxima of $F_r^{\max} = 1.42$ N vs. $F_m^{\max} = 2.36$ N. These interaction forces are very small in the context of robotic ultrasound scanning, and such controlled probe-tissue interaction is critical to avoid unnecessary brain tissue deformation.

Reproducible robotic scanning

Quantitative scan performance across all trials is summarized in Fig. 4a (boxplots of duration, coverage, symmetry, force, fan amplitude, and probe translation). The corresponding probe trajectories are shown in Fig. 4b-e. Manual acquisition was substantially faster ($t_m = 33.45 \pm 4.67$ s vs. $t_r = 128.22 \pm 2.88$ s). Notably, robotic scans additionally take approximately 50 s longer due to the initial surface normal identification phase, a step not required in manual operation. Both methods achieved comparable symmetry

[1]Consultant neuroradiologist at Imperial College Healthcare NHS Trust with extensive experience in intraoperative neurosurgical ultrasound

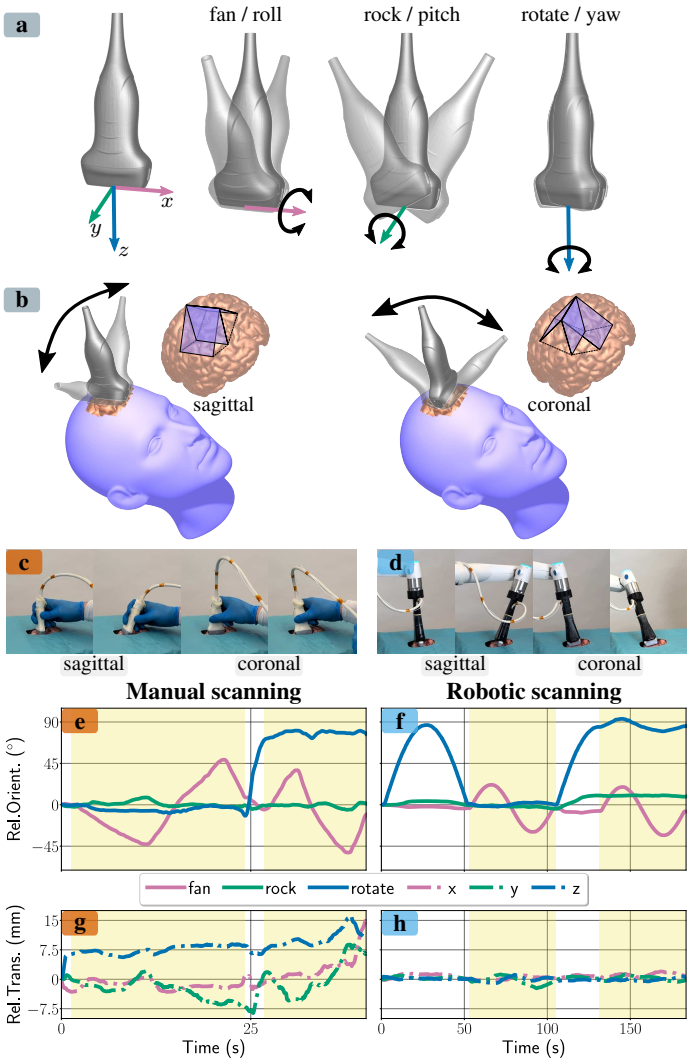

Fig. 2. **Ultrasound sweep scanning protocol.** (**a**) Reference coordinate system for probe rotations and translations. (**b**) Experiments were performed following a standard protocol, consisting of one fan motion in coronal plane, followed by the same motion in sagittal plane. Sequences of images show different moments throughout the scanning protocol with manual (**c**) and robotic (**d**) probe guidance. Recording of probe motions via electromagnetic tracking shows the three orientations in space ((**e**) manual scanning; (**f**) robotic scanning), as well as the amount of translation relative to the initial scanning point on the tissue ((**g**) manual scanning; (**h**) robotic scanning). Yellow shading in each plot highlights the two scanning phases in coronal and sagittal plane. An animated version of panels e,f alongside video recordings of robotic and manual scanning protocol executions and corresponding ultrasound images can be found in Extended Data, Movie E1.

($s_m = -0.01 \pm 0.03$, $s_r = -0.02 \pm 0.02$), indicating consistent perpendicular in-plane alignment. However, the robot achieved higher and more consistent coverage (mean $c_r = 0.82$ vs. $c_m = 0.46$; interquartile range (IQR) $\mathrm{IQR}(c_r) = 0.08$ vs. $\mathrm{IQR}(c_m) = 0.24$), demonstrating more stable coupling.

Interaction forces remained below 2 N within the 1.5-IQR range for both methods. Manual acquisition showed slightly lower and tighter forces ($|F_m| = 0.70 \pm 0.23$ N, $\mathrm{IQR}(|F_m|) = 0.32$ N, vs. $|F_r| = 0.90 \pm 0.41$ N, $\mathrm{IQR}(|F_r|) = 0.65$ N), a likely trade-off for the robot's higher coverage, which requires pushing deeper into the non-planar brain surface. The robot's greater force variance also stems from the limited craniotomy clearance: occasional probe-skull contact produces force spikes that a robot following a predefined protocol cannot avoid the way an expert sonographer intuitively does.

Manual guidance varied widely in fan amplitude ($\mathrm{IQR}(A_m^{\mathrm{fan}}) = 12.40°$) and speed, whereas the robotic scans were highly consistent ($\mathrm{IQR}(A_r^{\mathrm{fan}}) = 2.33°$) with near-perfect overlap of probe trajectories (Fig. 4b-e). This reproducibility is a critical advantage for integrating automated ultrasound into neurosurgical workflows.

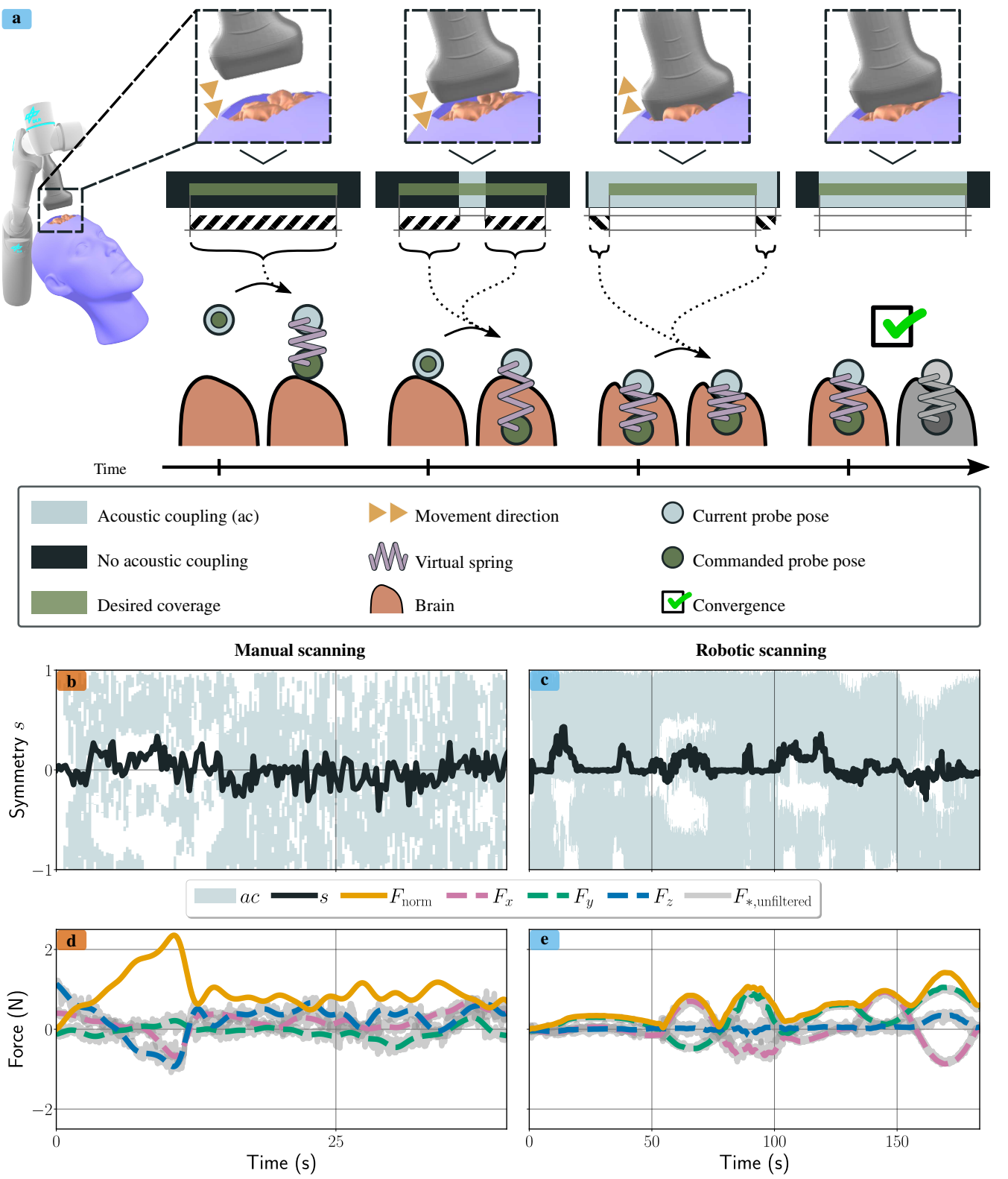

Fig. 3. **Acoustic coupling and probe-tissue interaction.** (**a**) The amount of acoustic coupling (coverage) controls how the robot adjusts the distance between ultrasound probe and brain tissue. A virtual spring between desired and actual probe position creates the interaction necessary for appropriate acoustic coupling. Here, acoustic coupling ac is visualized as light-blue shading for one manual (**b**) and one robotic (**c**) scan. The black line indicates the symmetry s of the probe-tissue coupling. Note that coupling and symmetry are plotted vertically over time, with the vertical axis spanning the width of the ultrasound image for ac or the range $[-1, 1]$ for s, respectively. Thus, each *column* of light-blue and white shading in panels b,c corresponds to one instance of acoustic coupling. (**d**) and (**e**) show the corresponding interaction forces generated between probe and tissue during each scan for manual and robotic acquisition, respectively. The results plotted here originate from the same experimental trial as was used in Fig. 2e-h. An animated version of panels b-e alongside video recordings of robotic and manual scanning protocol executions and corresponding ultrasound images can be found in Extended Data, Movie E1.

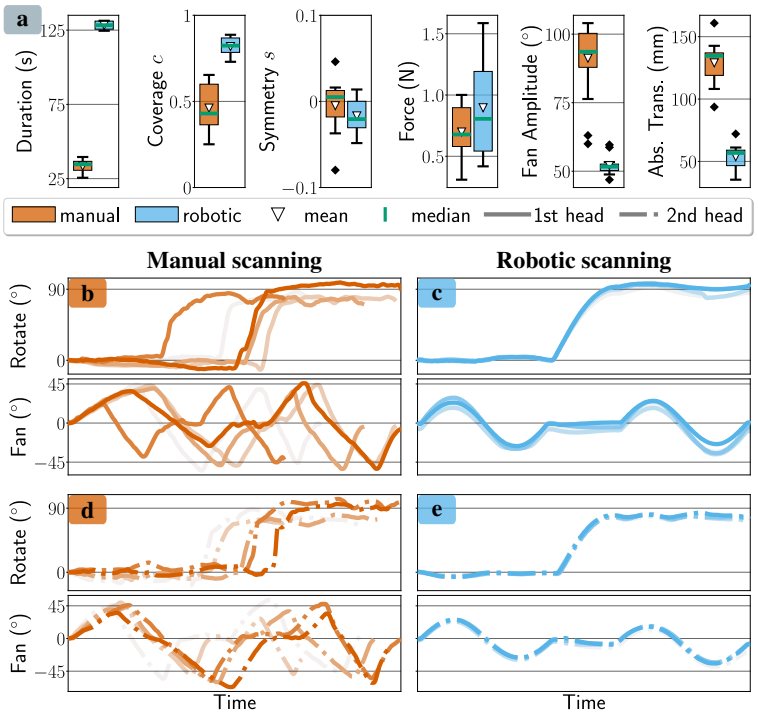

Fig. 4. **Inter-scan reproducibility.** (**a**) Analysis of quantitative metrics across repeated trials allows assessing scanning performance for manual (orange, $N_m = 10$) and robotic (blue, $N_r = 8$) image acquisition. Boxplots show the IQR (25th - 75th percentile) of each metric across scans, with whiskers extending to $\pm 1.5\times$IQR, and outliers highlighted as diamonds. Median (green line) and mean (triangle) complete the figure. The metrics include (from left to right) scanning duration, coverage and symmetry, force applied to the brain tissue, fan amplitude and absolute translation during the scanning. Probe rotation and fan motion for each trial are visualized in panels (**b**-**e**), again split between manual (**b, d**) and robotic (**c, e**) scanning. Different alpha values of each line color indicate different trials. Rotation trajectories were further divided into experiments on the first (**b, c**, $N_m^1 = 5$, $N_r^1 = 4$) and second (**d, e**, $N_m^2 = 5$, $N_r^2 = 4$) porcine head.

Trend toward superior image quality compared to expert scans

Anatomical landmarks including the cerebral cortex, lateral ventricles, thalamic nuclei, hippocampi, and basal ganglia were successfully captured across both manual (Fig. 5a,c) and robotic (Fig. 5b,d) acquisitions. This demonstrates that robotic scanning yields clinically relevant brain anatomy. To further validate image quality, eight medical experts (five neurosurgeons and three radiologists) from five clinical institutions rated the manual and robotic scans against ten quality criteria in a single-blind study (see Methods, Clinical image quality assessment). Results are presented in Fig. 6, showing reviewer-level mean ratings (averaged

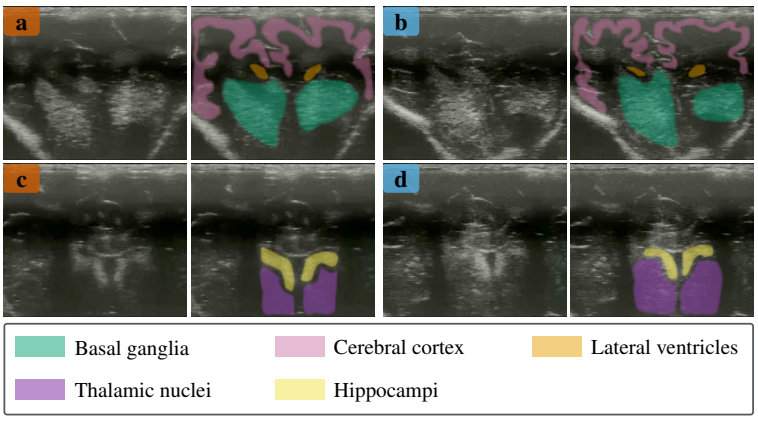

Fig. 5. **Example ultrasound images with manually segmented anatomical landmarks.** The images show different views on the porcine brain in coronal plane, both manually (**a, c**) and robotically (**b, d**) acquired, with highlighted important anatomical landmarks.

across recordings) for manual and robotic scans. Across all ten categories, mean ratings were higher for robotic scans, and medians showed the same tendency except for *a.* Anatomic coverage & completeness and *g.* Probe pressure/tissue deformation (visible). For *b.* Standard plane adequacy, the one-sided Wilcoxon signed-rank test on the paired robot-manual differences was as at the border of statistical significance (Holm-Bonferroni-adjusted $\mathrm{P_{holm}} = 0.0781$). All other categories showed no significant difference under neither the directional nor the exploratory two-sided analysis (all $\mathrm{P_{holm}} > 0.05$). However, seven of the ten criteria yielded moderate ($\rho_{\mathrm{rb}} \geq 0.5$) to large effect sizes ($\rho_{\mathrm{rb}} \geq 0.75$) favoring the robotic recordings. Taken together, these results show no evidence of a difference, with image quality indistinguishable from expert manual scans across the ten criteria, and indicate an overall trend toward superior quality of robotic scans. Detailed statistics, together with additional qualitative ratings of our expert sonographer, are provided in Extended Data A (Tables E1, E2, E3).

Autonomous scanning without preoperative mapping

Ultrasonic servoing achieves in-plane perpendicular alignment directly from the symmetry s of the acoustic coupling, relying exclusively on ultrasound image feedback. An asymmetric coupling ($s \neq 0$) drives a virtual rotational spring that turns the probe until the symmetry criterion ($s_{\mathrm{des}} = 0$) is met (Fig. 7a). During the subsequent rotation about the probe's longitudinal axis, an UKF estimates the full three-dimensional surface normal from the sequence of in-plane coupling measurements (Fig. 7b,d,e; details in Supplementary B). Because each coupling measurement informs only the in-plane component of the normal, the UKF uncertainties of the polar and azimuthal angles fluctuate anti-cyclically as the probe rotates. Throughout the rotation the controller maintains symmetrical coupling (Fig. 7c, $s_r = -0.05 \pm 0.10$), so the probe converges robustly to full perpendicular alignment with no prior geometric knowledge of the brain surface, i.e., without any preoperative mapping. Combined with surface-centric impedance control [37], the estimated normal lets the robot define probe orientation relative to the local surface geometry and execute any predefined rotational scanning protocol.

DISCUSSION

The primary achievement of this work is the simultaneous realization of safety and high image quality. We demonstrate the first autonomous robotic ultrasound scan of ex-vivo brain tissue with high-quality image acquisition at least comparable to expert manual scanning, achieving stable coupling and perpendicular alignment across repeated trials with minimal interaction forces on tissue as soft as the brain, providing a level of safety so far not reported in autonomous RUSS operating on organ tissue.

Looking at the clinical image quality assessment study, with only eight reviewers and correction across ten criteria, statistical significance requires at least one criterion to exhibit unanimous directional agreement across all reviewers. The absence of Holm-corrected significance in the results should therefore be considered in the context of this stringent statistical requirement rather than interpreted as evidence of an absence of systematic differences.

Achieving higher acoustic coverage usually comes at the expense of increased interaction forces. In manual scanning this trade-off is resolved implicitly by the operator and varies between individuals, whereas a robotic system enables explicit control of it, so the balance between coverage and force can be adapted to the clinical scenario. Strictly reaching a specific desired coverage (c_{des}) is, however, less critical. Of more importance is maintaining a higher and more consistent coverage than manual acquisition, as it is the stability of the probe-tissue interaction that prevents loss of acoustic coupling and the resulting artifacts. Still, the higher coverage achieved during robotic scanning should be interpreted in light of coverage being an explicit control objective of the robotic system. It is therefore, to some extent, expected by design. Nevertheless, the results demonstrate that this objective can be reliably translated into improved and more consistent probe-tissue coupling during scanning. The reported mean coverage should further be interpreted in anatomical context: fluid-filled structures such as the cerebral ventricles appear hypoechoic and may be classified as acoustic shadow (loss of coupling), as evident in Fig. 3b,c at $t_m \approx 8$ s (manual)

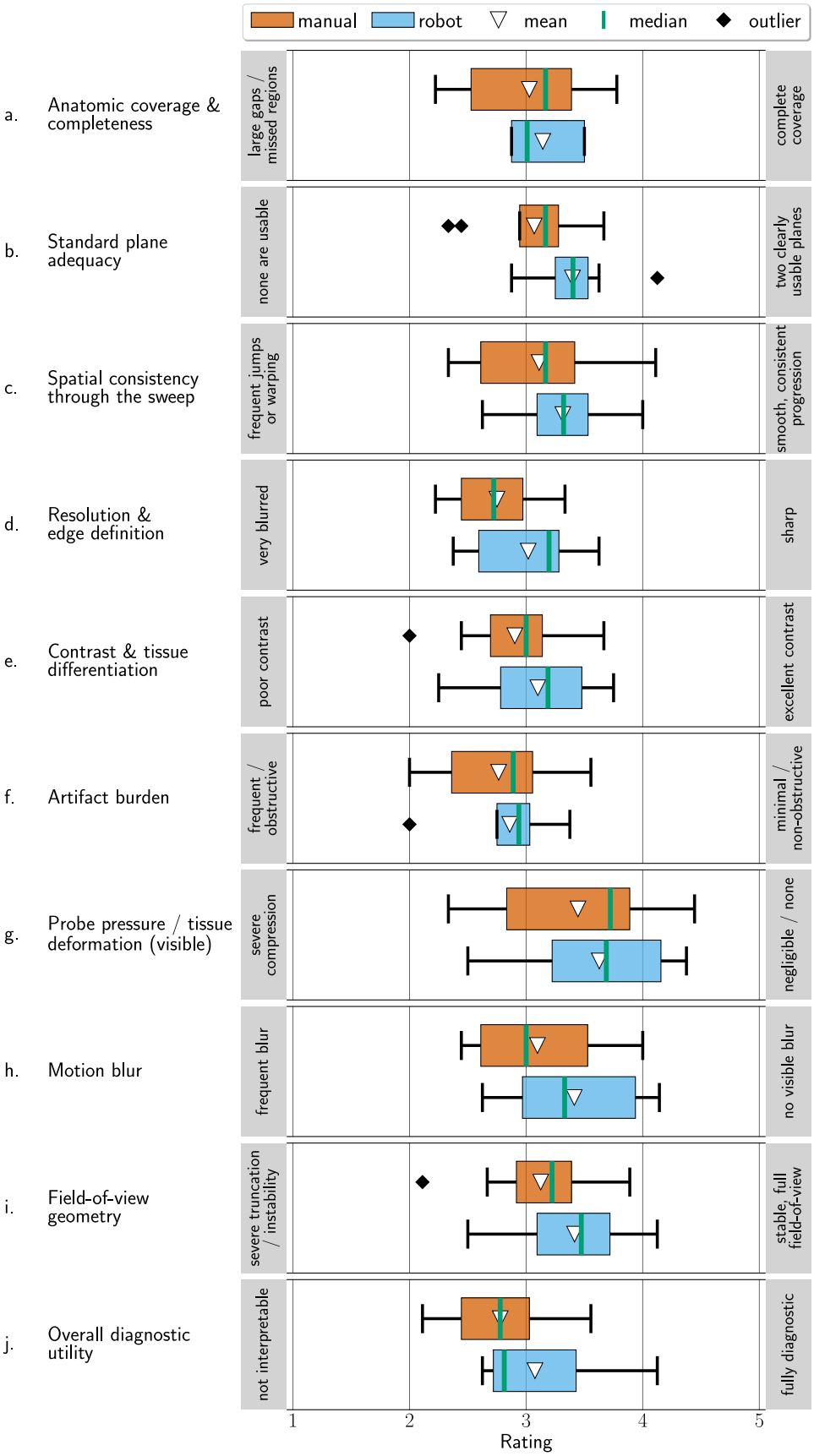

Fig. 6. **Ultrasound scan image quality assessment.** Medical experts assessed manually and robotically acquired ultrasound sweeps in a single-blind study. Boxplots show ratings across reviewers after averaging over all recordings, separated by method of image acquisition (manual: orange, robot: blue). Boxplots and whiskers follow the same visualization scheme as Fig. 4.

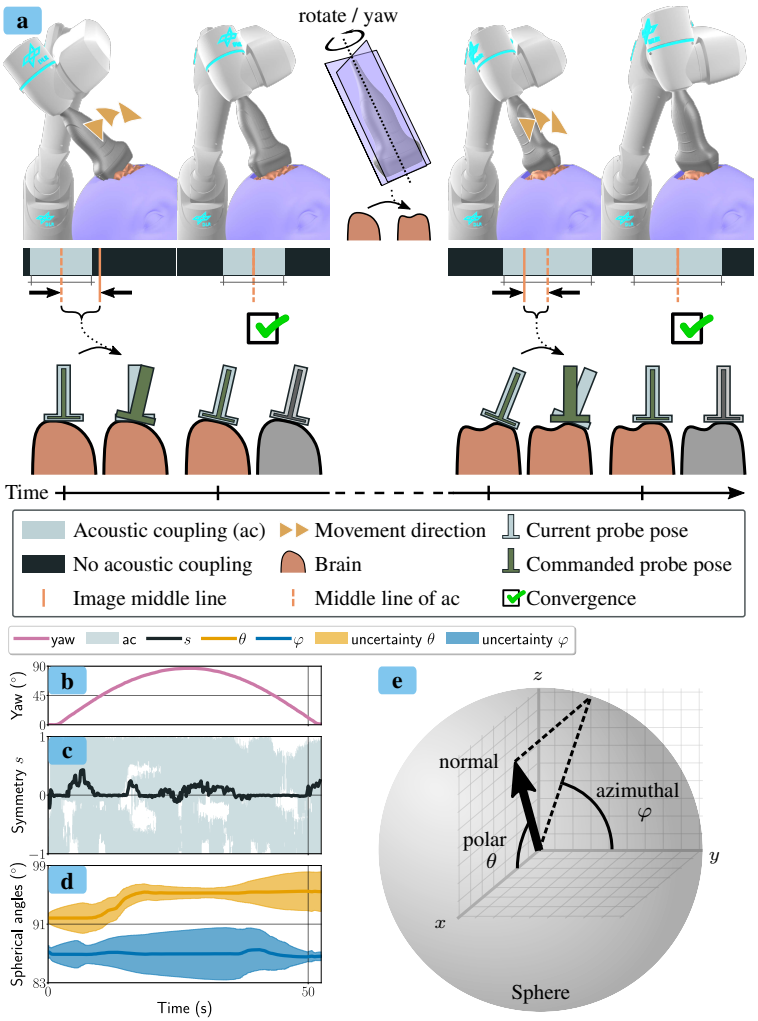

Fig. 7. **Probe orientation control.** (**a**) The robot uses acoustic coupling detection to derive symmetry of the contact between ultrasound probe and tissue. Asymmetrical contact results in a virtual rotational spring pulling the probe toward perpendicular alignment on the tissue surface in the current ultrasound plane. Rotating about the longitudinal axis of the probe while maintaining symmetrical coupling results in full perpendicular probe alignment. (**b**) Throughout this rotation (represented by the yaw angle) the UKF estimates the spherical coordinates (polar θ and azimuthal φ angles) (**d**) of the unknown tissue surface normal vector, visualized in (**e**). Colored shading indicates uncertainty of said observer. As seen in (**c**), the robot maintains symmetrical contact as well as possible throughout the rotation, resulting in overall perpendicular probe alignment.

and $t_r \approx 63$ s (robotic), where two contiguous regions classified as absence of acoustic coupling coincide with ventricular anatomy.

The interpretation of the symmetry criterion is inherently dependent on the level of coverage. While $s = 0$ at lower coverage provides strong evidence of a centered and approximately perpendicular probe-tissue interaction, the same value at high coverage is less informative. Consequently, the symmetry metric becomes less sensitive to deviations from perpendicularity as coverage increases.

Beyond safety, the quantitative analysis (Fig. 4) shows that robotic scanning eliminates the high intra-operator variability of manual ultrasound. The robot acquires sweeps at a smooth, constant rate, which is difficult to achieve manually, yielding consistent coverage and symmetry. This standardization eases interpretation for consulting neuroradiologists, reduces the risk of missed pathology from operator error or fatigue, simplifies documentation of resection progress, and, by lowering the variance in the input data, provides a sound foundation for AI-based image processing.

Finally, the autonomous surface-normal estimation removes the need for preoperative mapping or costly registration, and the relatively small footprint of our robotic arm (comparable to a human arm, ≈ 10 kg)

suggests that medical-product-certified systems could be integrated into surgery with little disruption to operative flow.

Despite these strengths, several trade-offs remain. Most notably, robotic scanning is currently slower than manual acquisition, primarily attributed to conservative velocity profiles that maximize safety and a roughly $50\ \mathrm{s}$ yaw rotation needed to identify the tissue normal and reach perpendicular alignment (limited by the rate of coupling measurements and filter iterations). In surgeries requiring short scans and quick views of the tissue, repeated robotic scanning adds extra time, potentially increasing the risk of complications. In clinical scenarios requiring prolonged imaging or in settings where expert sonographers are unavailable, this increased duration is offset by the guarantee of consistent, high-quality data. The fan range is also smaller than during manual scanning, and the protocol included no translational motion. In the clinical image quality assessment, robotic scans showed a larger IQR than manual scans for a few criteria. As the presented scores represent reviewer-level means averaged across recordings, this spread primarily reflects differences between reviewers. The larger IQR may therefore indicate greater inter-reviewer variability in the perception of specific image characteristics of the robotic acquisitions, particularly given the reviewer's familiarity with conventional manual ultrasound scanning. Finally, a sensitivity to surface contamination (fluids or debris) that can produce false-contact perception, remains to be addressed.

OUTLOOK

Several improvements are immediate. Translational motion is trivial to add within the surface-centric impedance coordinates to widen the fan field of view, and knowledge of the craniotomy size could be used to monitor the probe's relative position, so the available workspace is exploited fully without violating surgical boundaries. We anticipate that ongoing progress in low-latency sensing and high-bandwidth actuation will eventually reduce robotic scanning times. Robustness can also be improved: the stuttering at the fan and joint limits can be mitigated through better initial positioning and more advanced nullspace resolution techniques [39], and the sensitivity to surface contamination requires more robust image processing or complementary tactile analysis. Adapting the control to tissue deformation and varying tissue stiffness in real time should further homogenize image quality.

More ambitious extensions would use the stable, standardized data as a foundation for AI-based processing. Automated tumor detection and the derivation of probe poses to optimize intraoperative diagnosis would overcome the challenges of manual tumor segmentation [40], with phantom and animal studies generating the required training data and revealing new potentials and limitations. The ability to separate translation from rotation, a clear strength of a robotic arm, would also support more complex motion combinations driven by real-time image feedback, potentially through emerging approaches such as vision-language-action models (VLAs).

The generality of the approach is already suggested by its use beyond neurosurgery: in a parallel internal project we applied ultrasonic servoing to robotic ultrasound of the internal jugular vein, repeatedly scanning study subjects during the NASA/DLR *Sensorimotor Countermeasure Study - Campaign 3* bed-rest study in Cologne, Germany. Similarly, the controlled minimal-pressure operation could transfer to other stiffer, less sensitive tissues in diagnostic, interventional and operative ultrasound, such as obstetrics, breast, and vascular imaging. Synchronous live imaging during resection, for instance through a large craniotomy, dual craniotomies, or burr-holes [41, 42], is another promising scenario in which the robot could provide real-time anatomical feedback without the neurosurgeon shifting focus or relying on a sonographer's presence.

Ultimately, clinical translation will require evaluation in in-vivo surgical settings, including an assessment of the impact on extent of resection and survival. As robotic systems and their integration with other surgical technologies evolve, we expect the role of autonomous ultrasound scanning in neurosurgery to grow beyond the current demonstration phase toward routine clinical use.

METHODS

Experimental setup

The experimental setup is displayed in Fig. 8. Experiments were performed on ex-vivo porcine brain tissue using DLR MIRO [43], a seven degrees-of-freedom torque-controlled robotic manipulator equipped with a *GE 12L-RS* linear ultrasound probe, connected to a *GE LOGIQ e* ultrasound machine. The two porcine heads were prepared with a small craniotomy to simulate neurosurgical conditions and placed inside a box filled with ice to slow tissue degradation. An electromagnetic tracking system (*NDI Aurora®*) allowed precise measurement of probe poses, while a six degree-of-freedom force / torque sensor (*ATI Industrial Automation Mini45 Titanium*) with sensor resolution of roughly 0.03 to 0.06 N, mounted between two 3D-printed adapter plates, measured interaction forces and torques. The robotic controller runs at 3 kHz on a dedicated host, processing ultrasound images at 60 Hz.

Clinical image quality assessment

Image quality was assessed in a single-blind study by eight medical experts: five neurosurgeons and three radiologists (seven male, one female; ages 33, 34, 39, 43, 46, 46, 49, 52) from five clinical institutions (four in Germany, one in the UK). Written informed consent was obtained from all reviewers. Each reviewer rated their self-perceived level of expertise (R_{loe}) in brain ultrasound assessment on a 5-point Likert scale (1 = novice; 5 = expert). The resulting distribution, one novice ($R_{loe} = 1$), one beginner ($R_{loe} = 2$), three proficient users ($R_{loe} = 4$), and three experts ($R_{loe} = 5$), indicates a broad spectrum of experience among the participants. To assess the image quality of both manual and robotic scans, we use a qualitative scoring system with ten assessment criteria (see below), tailoring prior work [44–46] to intraoperative brain ultrasound. All robotic recordings were time-normalized to the duration of the manual recordings (approximately 30 to 35 seconds) to prevent reviewers from inferring the acquisition method from the scan duration. Before rating, all reviewers viewed a single manual recording as an example scan to familiarize themselves with the general image quality and porcine brain anatomy. This example was not rated, leaving $N_m = 9$ manual and $N_r = 8$ robotic recordings for evaluation.

Image quality assessment criteria

Ultrasound scans were evaluated across the following ten quality criteria, each scored on a 5-point Likert scale where higher scores indicate better performance:

1) **Anatomic coverage & completeness** Did the sweep capture the expected field (e.g., midline, deep nuclei, cortical surface) without major gaps? (1 = large gaps/missed regions; 5 = complete coverage)
2) **Standard plane adequacy** How well does the sweep include usable standard planes (e.g., midline/sagittal, coronal approximations)? (1 = none are usable; 5 = two clearly usable planes)
3) **Spatial consistency through the sweep** Are structures smoothly tracked without jumps/warps (slice spacing, probe motion)? (1 = frequent jumps/warping; 5 = smooth, consistent progression)
4) **Resolution & edge definition** Cortical/gyral margins and small structures have crisp boundaries. (1 = very blurred; 5 = sharp)
5) **Contrast & tissue differentiation** Parenchyma vs. CSF/ventricles/white-gray differentiation is clear. (1 = poor contrast; 5 = excellent contrast)
6) **Artifact burden** Shadowing, reverberation, dropout, mirror, saturation bars, or GUI overlays that obscure anatomy. (1 = artifacts frequently obscure anatomy; 5 = minimal/non-obstructive)
7) **Probe pressure / tissue deformation (visible)** Compression or distortion that alters anatomy. (1 = severe compression; 5 = negligible/none)
8) **Motion blur** From rapid sweep or instability. (1 = frequent blur; 5 = no visible blur)
9) **Field-of-view geometry** Sector/crop is stable; no truncation or variable windowing. (1 = severe truncation/instability; 5 = stable, full field-of-view)
10) **Overall diagnostic utility** (1 = not interpretable; 3 = borderline; 5 = fully diagnostic for typical neuro targets)

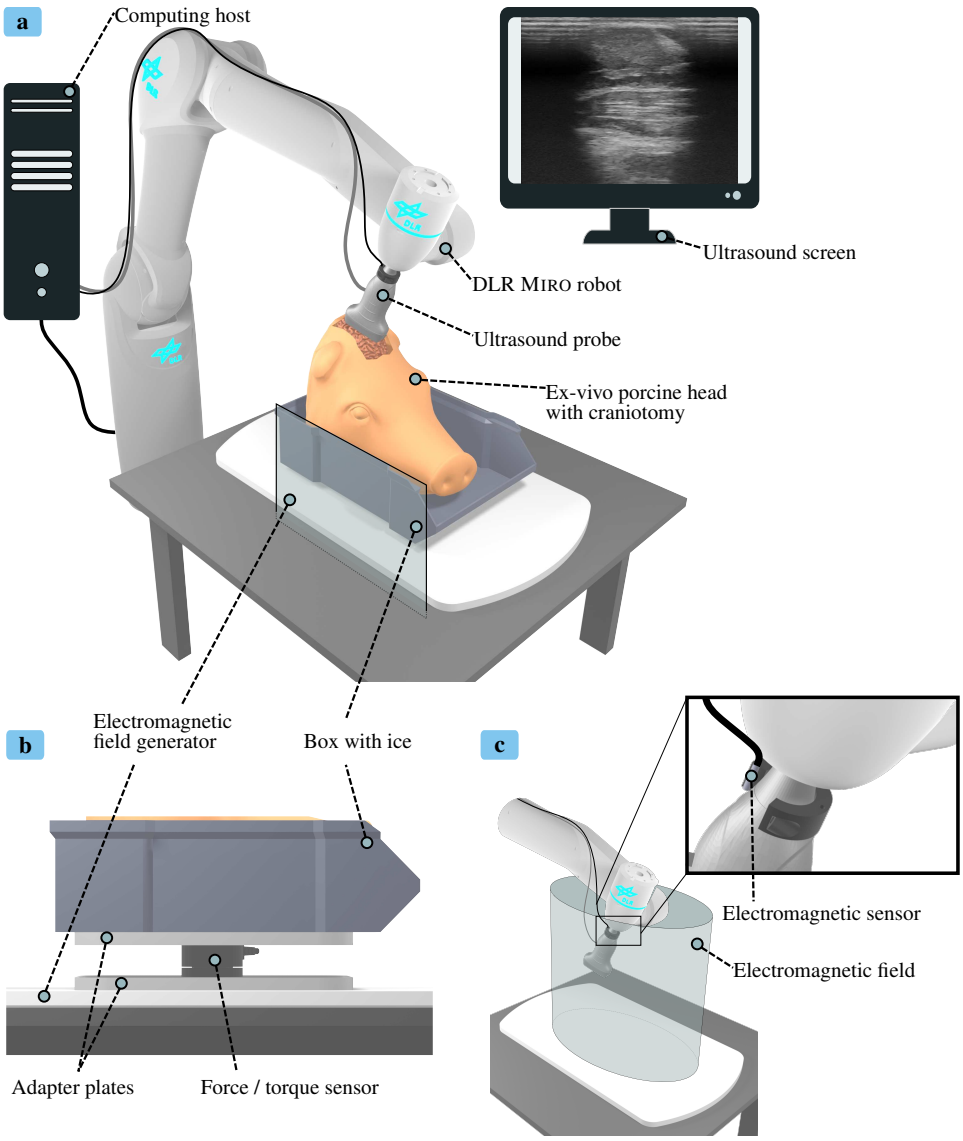

Fig. 8. **Experimental setup.** (**a**) Overview of the hardware involved in the robotic ultrasound scanning experiments. The DLR MIRO robot guides the ultrasound probe across the ex-vivo porcine brain, the ultrasound image is displayed on a screen. To avoid fast tissue degradation, the porcine head is placed inside a box filled with ice. Image processing and robotic control are executed on a dedicated host. The orthographic side view in (**b**) reveals a force / torque sensor (ATI Industrial Automation Mini45 Titanium) between two 3D-printed adapter plates to measure interaction forces and torques exerted on the tissue. (**c**) To track ultrasound probe motions during manual and robotic scans, an electromagnetic field generator (NDI Aurora®) recognizes motions of an electromagnetic sensor attached to the ultrasound probe.

Ultrasonic servoing control

This section introduces the ultrasonic servoing control cascade. Following the operational criteria defined earlier, we define a set of high-level objectives O:

- (O_1) Realization of a desired coverage $c_{\text{des}} \in [0, 1]$ to achieve stable acoustic coupling;
- (O_2) Symmetrical distribution ($s \in [-1, 1]$) of acoustic coupling ($s_{\text{des}} = 0$) to realize perpendicular probe alignment without prior knowledge of the surface geometry;
- (O_3) Identification of the normal vector of the tissue surface.

Acoustic coupling detection: To identify the probe-tissue contact quality, we use a method based on [36], which constructs a confidence map of the perceptual quality and detects contact-related acoustic shadow artifacts. This artifact is the most prevalent during intraoperative ultrasound, due to factors such as blood, poor contact and gas bubbles [9]. The algorithm detects acoustic coupling per scanline. With

this, objective O_1 becomes equivalent to realizing no contact-related acoustic shadowing artifacts across a desired fraction (given by c_{des}) of the width of the ultrasound image.

Mathematically, the algorithm detecting acoustic coupling in a linear ultrasound image $\boldsymbol{\mathcal{I}}_{(w\times h)}$ of width w and height h is a map

$$g_{ac} : \boldsymbol{\mathcal{I}}_{(w\times h)} \mapsto \boldsymbol{a} = g_{ac}(\boldsymbol{\mathcal{I}}_{(w\times h)}), \tag{1}$$

with $\boldsymbol{a} \in \{0,1\}^w$ the binary w-tuple

$$a_i = \begin{cases} 1 & \text{if acoustic coupling along scanline } i, \\ 0 & \text{otherwise,} \end{cases} \tag{2}$$

for $i \in \{1,\dots,w\}$. The two main metrics extracted from the ultrasound image that drive the ultrasonic servoing control, coverage $c \in [0,1]$ and symmetry $s \in [-1,1]$, can then be calculated as

$$c = {}^1\!/_w \sum_{i=1}^{w} a_i, \quad s = {}^2\!/_w \sum_{i=1}^{w} \begin{cases} -a_i & \text{if } i < {}^w\!/_2 \\ +a_i & \text{if } i > {}^w\!/_2 \end{cases}. \tag{3}$$

Then, objective O_2 can be rephrased as

($O_{2.1}$) $\boldsymbol{a}$ should be symmetrically distributed around the center of the ultrasound image, i.e., $s = 0$;

($O_{2.2}$) $O_{2.1}$ holds for all $\beta \in [-{}^\pi\!/_2; {}^\pi\!/_2]$.

Here, β is the yaw angle of the ultrasound probe. We introduce objective $O_{2.2}$ as the symmetry of $\boldsymbol{a}$ can only provide information on the in-plane orientation of the ultrasound probe for a given β. Hence, achieving a symmetric distribution of $\boldsymbol{a}$ ($s = 0$) for all β ensures a probe alignment normal to the brain tissue, and thus $O_2 = O_{2.1} \wedge O_{2.2}$. Now, given (2) and (3), objectives O_1 and $O_{2.1}$ become equivalent to realizing a desired coverage c_{des}, or in other words a desired tuple $\boldsymbol{a}_{\text{des}}$ with elements $a_{\text{des},i}$ that satisfy

$$\begin{aligned} c_{\text{des}} &= {}^1\!/_w \sum_{i=1}^{w} a_{\text{des},i} \\ s_{\text{des}} &= {}^2\!/_w \sum_{i=1}^{w} \begin{cases} -a_{\text{des},i} & \text{if } i < {}^w\!/_2 \\ +a_{\text{des},i} & \text{if } i > {}^w\!/_2 \end{cases}. \end{aligned} \tag{4}$$

Surface-centric impedance control: Surface-centric impedance control [37] allows controlling a tool relative to an arbitrary surface. Let $\boldsymbol{x}_t = (x_t\ y_t\ z_t)^\mathsf{T} \in \mathbb{R}^3$ be the translational component of the Cartesian forward kinematics $f_{\text{kin}} : \mathcal{Q} \to SE(3) \mid \boldsymbol{q} \mapsto \boldsymbol{x} = f_{\text{kin}}(\boldsymbol{q})$, i.e., the pose of the ultrasound probe, where $\boldsymbol{q} \in \mathcal{Q}$ represent generalized configuration coordinates of the robot. The impedance controller [37] realizes a virtual spring-damper system in surface-centric task coordinates

$$\boldsymbol{\rho} = \begin{pmatrix} d(\boldsymbol{q}) \\ \boldsymbol{\epsilon}(\boldsymbol{q}) \end{pmatrix} \in \mathbb{R}^4, \tag{5}$$

where d is the signed distance between the ultrasound probe and the surface, and $\boldsymbol{\epsilon} \in \mathbb{R}^3$ describes the orientational deviation from the surface normal.

Using (5) we implement an operational space impedance control law [47, 48]

$$\boldsymbol{\tau} = \boldsymbol{J}_\rho^\mathsf{T}(\boldsymbol{q})[\boldsymbol{K}_\rho(\boldsymbol{\rho}_{\text{des}} - \boldsymbol{\rho}(\boldsymbol{q})) + \boldsymbol{D}_\rho(\boldsymbol{q})(\dot{\boldsymbol{\rho}}_{\text{des}} - \boldsymbol{J}_\rho(\boldsymbol{q})\dot{\boldsymbol{q}})], \tag{6}$$

with $\boldsymbol{\tau} \in \mathbb{R}^n$ being the desired joint torques of an n-degrees of freedom, torque-controlled manipulator. The term $\boldsymbol{J}_\rho(\boldsymbol{q}) \in \mathbb{R}^{4\times n}$ denotes the Jacobian of $\boldsymbol{\rho}(\boldsymbol{q})$, i.e., the product $\boldsymbol{J}_\rho = \boldsymbol{J}_{\rho x}\boldsymbol{J}_x$ of the known geometrical Jacobian $\dot{\boldsymbol{x}} = \begin{bmatrix}\boldsymbol{v} & \boldsymbol{\omega}\end{bmatrix}^\mathsf{T} = \boldsymbol{J}_x(\boldsymbol{q})\dot{\boldsymbol{q}}$ and the Jacobian of $\boldsymbol{\rho}(\boldsymbol{x})$.

Specifying $\boldsymbol{\rho}_{\text{des}} \in \mathbb{R}^4$ allows controlling the distance of the ultrasound probe to the tissue surface and the probe orientation relative to the surface normal. Perpendicular alignment of the probe is achieved through $\boldsymbol{\epsilon}_{\text{des}} = \boldsymbol{0}$. Establishment of contact initiates at $d_{\text{des}} = 0$, for direct interaction with the tissue $d_{\text{des}} < 0$. The resulting passive contact forces depend on the value of d_{des}, as well as on the controller and object stiffnesses.

Ultrasonic servoing control: To accomplish objectives O_1-O_3 we combine acoustic coupling detection, surface-centric impedance control and a state observer estimating the local tissue geometry.
The innermost control loop controls the robot manipulator, with torques $\boldsymbol{\tau}$ provided by the surface-centric impedance controller. In the outer loop, the surface geometry observer, based on an UKF [49], reads measurements (coverage and symmetry) from the ultrasound image and updates the local tissue surface estimate. The surface-centric impedance control then calculates the torques necessary to move the ultrasound probe relative to the estimated surface.
What remains is to specify a desired distance to achieve a certain interaction. We propose setting the desired distance based on a desired coverage $c_{\mathrm{des}} \in [0, 1]$. As visualized in Fig. 3, the reference point of the surface-centric impedance controller is placed below the brain tissue surface to achieve coupling between probe and tissue. A *coverage controller* takes care of commanding a distance $d_{\mathrm{des}} < 0$ that results in the surface-centric impedance controller converging to an equilibrium where $c = c_{\mathrm{des}}$. Details can be found in Supplementary B.

The robot guiding the ultrasound probe can be initialized arbitrarily above the target tissue. The UKF is initialized to a state aligning the surface normal vector with the probe's longitudinal axis. When establishing contact, the UKF updates its state estimate, and the ultrasonic servoing controller orients the probe and adjusts the penetration depth. Rotation of the ultrasound probe (cf. Fig. 7 and objective $O_{2.2}$) initiates automatically after perpendicular in-plane orientation is reached.

Statistical analysis

Ratings were averaged across recordings separately for each reviewer, acquisition method, and quality criteria, resulting in one paired robot and manual score per reviewer and criterion. Paired differences were calculated as the reviewer-level mean rating for robotic acquisition minus the corresponding mean rating for manual acquisition. Nonparametric testing was used because ratings originated from a five-point Likert scale and the number of reviewers was small. The directional hypothesis that robotic acquisition received higher ratings than manual acquisition was evaluated using one-sided Wilcoxon signed rank tests. Two-sided Wilcoxon signed rank tests were additionally conducted as exploratory analyses to assess differences irrespective of direction. To control the alpha inflation by multiple testing across the ten quality criteria, all P values were adjusted using the Holm-Bonferroni procedure, separately for the primary one-sided and exploratory two-sided tests. Effect sizes were quantified using matched-pairs rank-biserial correlations, with positive values indicating higher ratings for robotic acquisition. Statistical significance was defined as a Holm-Bonferroni-adjusted P value below 0.05.

REFERENCES

[1] R. L. Siegel, K. D. Miller, N. S. Wagle, and A. Jemal, "Cancer statistics, 2023," *CA: a cancer journal for clinicians*, vol. 73, no. 1, pp. 17–48, 2023.

[2] N. Burnet, S. Jefferies, R. Benson, D. Hunt, and F. Treasure, "Years of life lost (yll) from cancer is an important measure of population burden—and should be considered when allocating research funds," *British journal of cancer*, vol. 92, no. 2, pp. 241–245, 2005.

[3] S. Lapointe, A. Perry, and N. A. Butowski, "Primary brain tumours in adults," *The Lancet*, vol. 392, no. 10145, pp. 432–446, 2018.

[4] J. P. Almeida, K. L. Chaichana, J. Rincon-Torroella, and A. Quinones-Hinojosa, "The value of extent of resection of glioblastomas: Clinical evidence and current approach," *Current neurology and neuroscience reports*, vol. 15, pp. 1–13, 2015.

[5] H. Duffau, "Long-term outcomes after supratotal resection of diffuse low-grade gliomas: A consecutive series with 11-year follow-up," *Acta neurochirurgica*, vol. 158, pp. 51–58, 2016.

[6] S. L. Hervey-Jumper and M. S. Berger, "Maximizing safe resection of low- and high-grade glioma," *Journal of Neuro-Oncology*, vol. 130, pp. 269–282, 2016.

[7] I. J. Gerard, M. Kersten-Oertel, K. Petrecca, D. Sirhan, J. A. Hall, and D. L. Collins, "Brain shift in neuronavigation of brain tumors: A review," *Medical image analysis*, vol. 35, pp. 403–420, 2017.

[8] C. M. Rumack and D. Levine, Eds., *Diagnostic Ultrasound*, 6th ed. Philadelphia, PA: Elsevier, 2023, ISBN: 9780323877954.

[9] L. Dixon, A. Lim, M. Grech-Sollars, D. Nandi, and S. J. Camp, "Intraoperative ultrasound in brain tumor surgery: A review and implementation guide," *Neurosurgical Review*, vol. 45, pp. 2503–2515, 2022.

[10] M. A. Pino et al., "New hope in brain glioma surgery: The role of intraoperative ultrasound. a review," *Brain Sciences*, vol. 8, no. 11, p. 202, 2018.

[11] S. Mahboob et al., "Intraoperative ultrasound-guided resection of gliomas: A meta-analysis and review of the literature," *World Neurosurgery*, vol. 92, pp. 255–263, 2016, ISSN: 1878-8750.

[12] G. J. Dohrmann and J. M. Rubin, "History of intraoperative ultrasound in neurosurgery," *Neurosurgery Clinics*, vol. 12, no. 1, pp. 155–166, 2001.

[13] G. Unsgaard, S. Ommedal, T. Muller, A. Gronningsaeter, and T. A. Nagelhus Hernes, "Neuronavigation by intraoperative three-dimensional ultrasound: Initial experience during brain tumor resection," *Neurosurgery*, vol. 50, no. 4, pp. 804–812, 2002.

[14] R. Sastry et al., "Applications of ultrasound in the resection of brain tumors," *Journal of Neuroimaging*, vol. 27, no. 1, pp. 5–15, 2017.

[15] G. Trevisi, P. Barbone, G. Treglia, M. V. Mattoli, and A. Mangiola, "Reliability of intraoperative ultrasound in detecting tumor residual after brain diffuse glioma surgery: A systematic review and meta-analysis," *Neurosurgical review*, vol. 43, no. 5, pp. 1221–1233, 2020.

[16] G. R. Giammalva et al., "Intraoperative ultrasound: Emerging technology and novel applications in brain tumor surgery," *Frontiers in Oncology*, vol. 12, p. 818 446, 2022, ISSN: 2234-943X.

[17] C. de Quintana-Schmidt et al., "Neuronavigated ultrasound in neuro-oncology: A true real-time intraoperative image," *World Neurosurgery*, vol. 157, e316–e326, 2022, ISSN: 1878-8750.

[18] W. A. Berg, J. D. Blume, J. B. Cormack, and E. B. Mendelson, "Operator dependence of physician-performed whole-breast us: Lesion detection and characterization," *Radiology*, vol. 241, no. 2, pp. 355–365, 2006.

[19] A. M. Priester, S. Natarajan, and M. O. Culjat, "Robotic ultrasound systems in medicine," *IEEE Transactions on Ultrasonics, Ferroelectrics, and Frequency Control*, vol. 60, no. 3, pp. 507–523, 2013.

[20] Z. Jiang, S. E. Salcudean, and N. Navab, "Robotic ultrasound imaging: State-of-the-art and future perspectives," *Medical image analysis*, vol. 89, p. 102 878, 2023.

[21] R. Elek et al., "Robotic platforms for ultrasound diagnostics and treatment," in *2017 IEEE International Conference on Systems, Man, and Cybernetics (SMC)*, 2017, pp. 1752–1757.

[22] D. R. Swerdlow, K. Cleary, E. Wilson, B. Azizi-Koutenaei, and R. Monfaredi, "Robotic arm-assisted sonography: Review of technical developments and potential clinical applications," *American Journal of Roentgenology*, vol. 208, no. 4, pp. 733–738, 2017.

[23] K. Li, Y. Xu, and M. Q.-H. Meng, "An overview of systems and techniques for autonomous robotic ultrasound acquisitions," *IEEE Transactions on Medical Robotics and Bionics*, vol. 3, no. 2, pp. 510–524, 2021.

[24] M. G. Lubner, L. Mankowski Gettle, D. H. Kim, T. J. Ziemlewicz, N. Dahiya, and P. Pickhardt, "Diagnostic and procedural intraoperative ultrasound: Technique, tips and tricks for optimizing results," *British Journal of Radiology*, vol. 94, no. 1121, p. 20 201 406, May 2021, ISSN: 1748-880X.

[25] C. F. Guimarães, L. Gasperini, A. P. Marques, and R. L. Reis, "The stiffness of living tissues and its implications for tissue engineering," *Nature Reviews Materials*, vol. 5, no. 5, pp. 351–370, 2020.

[26] S. Virga et al., "Automatic force-compliant robotic ultrasound screening of abdominal aortic aneurysms," in *2016 IEEE/RSJ International Conference on Intelligent Robots and Systems (IROS)*, 2016, pp. 508–513.

[27] O. Zettinig et al., "3d ultrasound registration-based visual servoing for neurosurgical navigation," *International journal of computer assisted radiology and surgery*, vol. 12, pp. 1607–1619, 2017.

[28] F. Suligoj, C. M. Heunis, J. Sikorski, and S. Misra, "Robust–an autonomous robotic ultrasound system for medical imaging," *IEEE Access*, vol. 9, pp. 67 456–67 465, 2021.

[29] Q. Huang, J. Lan, and X. Li, "Robotic arm based automatic ultrasound scanning for three-dimensional imaging," *IEEE Transactions on Industrial Informatics*, vol. 15, no. 2, pp. 1173–1182, 2019.

[30] X. Ma, W.-Y. Kuo, K. Yang, A. Rahaman, and H. K. Zhang, "A-see: Active-sensing end-effector enabled probe self-normal-positioning for robotic ultrasound imaging applications," *IEEE Robotics and Automation Letters*, vol. 7, no. 4, pp. 12 475–12 482, 2022.

[31] A. Karamalis, W. Wein, T. Klein, and N. Navab, "Ultrasound confidence maps using random walks," *Medical image analysis*, vol. 16 6, pp. 1101–12, 2012.

[32] P. Chatelain, A. Krupa, and N. Navab, "Optimization of ultrasound image quality via visual servoing," in *2015 IEEE International Conference on Robotics and Automation (ICRA)*, 2015, pp. 5997–6002.

[33] P. Chatelain, A. Krupa, and N. Navab, "Confidence-driven control of an ultrasound probe," *IEEE Transactions on Robotics*, vol. 33, no. 6, pp. 1410–1424, 2017.

[34] M. Welleweerd, A. de Groot, S. de Looijer, F. Siepel, and S. Stramigioli, "Automated robotic breast ultrasound acquisition using ultrasound feedback," in *2020 IEEE International Conference on Robotics and Automation (ICRA)*, 2020, pp. 9946–9952.

[35] Z. Jiang, M. Grimm, M. Zhou, Y. Hu, J. Esteban, and N. Navab, "Automatic force-based probe positioning for precise robotic ultrasound acquisition," *IEEE Transactions on Industrial Electronics*, vol. 68, no. 11, pp. 11 200–11 211, 2021.

[36] A. Weld et al., "Identifying visible tissue in intraoperative ultrasound: A method and application," *International Journal of Computer Assisted Radiology and Surgery*, vol. 20, no. 10, pp. 2107–2117, 2025.

[37] M. Dyck, A. Sachtler, J. Klodmann, and A. Albu-Schäffer, "Impedance control on arbitrary surfaces for ultrasound scanning using discrete differential geometry," *IEEE Robotics and Automation Letters*, vol. 7, no. 3, pp. 7738–7746, 2022.

[38] M. Dyck et al., "Toward safe and collaborative robotic ultrasound tissue scanning in neurosurgery," *IEEE Transactions on Medical Robotics and Bionics*, vol. 6, no. 1, pp. 64–67, 2024.

[39] A. Dietrich and C. Ott, "Hierarchical impedance-based tracking control of kinematically redundant robots," *IEEE Transactions on Robotics*, vol. 36, no. 1, pp. 204–221, 2020.

[40] A. Weld et al., "Challenges with segmenting intraoperative ultrasound for brain tumours," *Acta Neurochirurgica*, vol. 166, no. 1, p. 317, 2024, ISSN: 0942-0940.

[41] I. Kanazawa, K. Shiraishi, H. Kamitani, J. Sato, and H. Masuzawa, "Intraoperative ultrasonography through a burr hole: Clinical trial of ultrasound-guided stereotactic surgery," *No Shinkei geka. Neurological Surgery*, vol. 14, no. 3 Suppl, pp. 295–300, 1986.

[42] G. Unsgaard, A. Kleven, S. Ommedal, and A. Gronningsaeter, "An ultrasound-based neuronavigation system, a good solution to the brain-shift problem," *Neurosurgery*, vol. 10, pp. 00 006 123–199 909 000, 1999.

[43] U. Seibold, B. Kübler, T. Bahls, R. Haslinger, and F. Steidle, "The dlr mirosurge surgical robotic demonstrator," in *The Encyclopedia of Medical Robotics*. World Scientific, 2019, ch. Chapter 5, pp. 111–142.
[44] D. Aleo et al., "Evaluation of a navigated 3d ultrasound integration for brain tumor surgery: First results of an ongoing prospective study," *Current Oncology*, vol. 29, no. 9, pp. 6594–6609, 2022, ISSN: 1718-7729.
[45] A. McDonald-Bowyer, T. Syer, A. Retter, D. Stoyanov, and A. Stilli, "Autonomous control of an ultrasound probe for intra-operative ultrasonography using vision-based shape sensing of pneumatically attachable flexible rails," *International Journal of Computer Assisted Radiology and Surgery*, vol. 19, no. 7, pp. 1391–1398, 2024, ISSN: 1861-6429.
[46] H. M. S. S. Herath, H. M. K. K. M. B. Herath, N. Madusanka, and B.-I. Lee, "A systematic review of medical image quality assessment," *Journal of Imaging*, vol. 11, no. 4, 2025, ISSN: 2313-433X.
[47] N. Hogan, "Impedance control: An approach to manipulation," in *1984 American Control Conference*, 1984, pp. 304–313.
[48] O. Khatib, "A unified approach for motion and force control of robot manipulators: The operational space formulation," *IEEE Journal on Robotics and Automation*, vol. 3, no. 1, pp. 43–53, 1987.
[49] E. Wan and R. Van Der Merwe, "The unscented kalman filter for nonlinear estimation," in *Proceedings of the IEEE 2000 Adaptive Systems for Signal Processing, Communications, and Control Symposium (Cat. No.00EX373)*, 2000, pp. 153–158.

ACKNOWLEDGEMENTS

The experimental protocol of the single-blind study in this work was approved by a DLR ethics committee ("DLR Office for Research Ethics"; Sign: 28/26). We would like to thank all medical experts and their clinical institutions that participated in the study. We appreciate their time taken and their support in evaluating our robotic system. A large language model (LLM) (Qwen 3.6 (qwen3.6:35b-a3b-q8_0)) via a DLR-hosted Ollama server instance was used only to assist during preparation of the manuscript, not during the actual research. The LLM was used to refine, correct or edit existing text and improve language, and to assist in writing code for the evaluation of study results and plotting of data. No figures in the manuscript were generated, refined, edited or corrected by the LLM.

FUNDING

Funding was provided by the Institute of Robotics and Mechatronics, German Aerospace Center (DLR) to M.D., A.K., B.W., A.D., J.K., A.A.-S.. M.D. was additionally supported by the International Graduate School of Science and Engineering (IGSSE); Technical University of Munich (TUM) Graduate School. A.S. was funded by the Free State of Bavaria through institutional funds from the School of Computation, Information, and Technology (CIT) at the Technical University of Munich (TUM). A.W. was funded by the UK Research and Innovation (UKRI) Centre for Doctoral Training in AI for Healthcare (EP/S023283/1). S.G. was funded by the Royal Society [URF \R \201014]. L.D. was funded by the NIHR Imperial Biomedical Research Centre and The R.L.ST.J. Harmsworth Memorial Research Fund.

DATA AND MATERIALS AVAILABILITY

All data needed to evaluate the conclusions in the paper are present in the paper, the attached Extended Data Tables, and in a repository deposited to figshare, accessible under https://doi.org/10.6084/m9.figshare.33723628. The deposited data include an example questionnaire as presented to the subjects, the questionnaire data, and the experiment logs. The questionnaire data contain the ratings of the medical experts for each of the ten quality criteria, for each of the manual and robotic ultrasound image acquisition runs, and are available as Excel file (raw data) and Python pickle file (parsed data). The experiment logs contain the time-series data for the robotic experiments, including the ultrasound images, robot state, joint positions, Cartesian poses, and force/torque measurements. For the manual ultrasound acquisition runs performed by the medical expert, the time-series data comprise the ultrasound images, the electromagnetic tracking data of the probe, and the force/torque measurements. The experiment logs are available as HDF5 files. We also provide videos of the experiments and videos of the ultrasound image stream for each of the manual and robotic runs. The data repository also contains the source data (parsed from the raw experiment logs) used to generate the manuscript figures (cf. Extended Data C).

Code availability

The code used to analyze and visualize the experiment data and questionnaire data is available at the same figshare repository https://doi.org/10.6084/m9.figshare.33723628. It performs the statistical analysis of the questionnaire data and generates the plots and visualizations shown in this paper, including the figures. While the paper shows experimental data for selected robotic and manual runs, the code additionally allows users to (1) reproduce these figures and (2) visualize the data for all other runs. The code is provided as Python scripts.

Author contributions

M.D., A.S. and J.K. generated and formulated the proposed methodology and mathematical foundation. M.D. implemented the system, performed the experiments, analyzed the data, wrote the paper and is the main author. L.D., A.K. and A.W. supported in preparing and performing the experiments. L.D. served as medical expert, performed part of the experiments himself, and provided input on all medical topics within the paper. L.D., A.W. and S.C. were responsible for clinical translation and any medically focused developments within the project. A.K. supported in mechanical and hardware topics to have a running demonstrator. B.W. supported in data analysis and statistical evaluation of results. S.G. contributed to the project conception and idea and provided funding. J.K. and A.A.-S. led the project, generated and formulated the project ideas, revised the manuscript and provided funding. A.D. and A.S. revised the manuscript and supported in drafting the paper.

Competing interests

The following patent applications related to this work have been filed: German patent application 2025062123450627DE, international patent application PCT/EP2026/068315 (M.D., A.S., J.K., A.A.-S.).

EXTENDED DATA A
TABLES FOR STATISTICAL ANALYSIS

TABLE E1
COMPARISON OF REVIEWER RATINGS ACROSS MANUAL ($N_m = 9$) AND ROBOTIC ($N_r = 8$) ULTRASOUND ACQUISITIONS OVER TEN CLINICAL IMAGE QUALITY CRITERIA. RATINGS WERE AVERAGED ACROSS RECORDINGS SEPARATELY FOR EACH REVIEWER AND ACQUISITION METHOD. THE MAPPING BETWEEN LETTERS AND QUALITY CRITERIA CAN BE FOUND IN FIG. 6 AND THE METHODS SECTION OF THE MAIN MANUSCRIPT.

Criterion	Mean rating		Std rating		Median rating	
	manual	robot	manual	robot	manual	robot
a.	3.0278	3.1429	0.5292	0.2893	3.1667	3.0089
b.	3.0694	3.3973	0.4301	0.3774	3.1667	3.4018
c.	3.1111	3.3147	0.5774	0.3992	3.1667	3.3214
d.	2.7500	3.0179	0.3716	0.4265	2.7222	3.1964
e.	2.9028	3.1004	0.4728	0.5031	3.0000	3.1875
f.	2.7639	2.8594	0.5075	0.3773	2.8889	2.9375
g.	3.4444	3.6272	0.6804	0.6169	3.7222	3.6875
h.	3.0972	3.4129	0.5650	0.5422	3.0000	3.3304
i.	3.1250	3.4152	0.5135	0.5013	3.2222	3.4732
j.	2.7778	3.0759	0.4231	0.5011	2.7778	2.8125

TABLE E2
STATISTICAL COMPARISON OF MANUAL ($N_m = 9$) VERSUS ROBOTIC ($N_r = 8$) ULTRASOUND ACQUISITIONS ACROSS TEN CLINICAL IMAGE QUALITY CRITERIA. RAW P VALUES (P_{RAW}) OF ONE-SIDED (ROBOT > MANUAL) AND TWO-SIDED WILCOXON (W) SIGNED RANK TESTS WERE ADJUSTED USING THE HOLM-BONFERRONI PROCEDURE (P_{holm}). EFFECT SIZES ρ_{RB} WERE QUANTIFIED USING MATCHED-PAIRS RANK-BISERIAL CORRELATIONS. THE MAPPING BETWEEN LETTERS AND QUALITY CRITERIA CAN BE FOUND IN FIG. 6 AND THE METHODS SECTION OF THE MAIN MANUSCRIPT.

Crit.	One-sided testing			Two-sided testing			Effect size
	W	P_{raw}	P_{holm}	W	P_{raw}	P_{holm}	ρ_{rb}
a.	23	0.2617	0.5391	13	0.5234	1.0000	0.2778
b.	35	0.0078	0.0781	1	0.0156	0.1562	0.9444
c.	27	0.1211	0.4844	9	0.2422	0.9688	0.5000
d.	30	0.0508	0.4062	6	0.1016	0.8125	0.6667
e.	23	0.0781	0.4688	5	0.1562	0.9375	0.6429
f.	16	0.3594	0.5391	11.5	0.7188	1.0000	0.1786
g.	25	0.1797	0.5391	11	0.3594	1.0000	0.3889
h.	28	0.0898	0.4688	8	0.1797	0.9375	0.5556
i.	31	0.0312	0.2812	4.5	0.0625	0.5625	0.7500
j.	30	0.0547	0.4062	6	0.1094	0.8125	0.6667

TABLE E3
MEDICAL EXPERT ASSESSMENT OF ROBOTIC ULTRASOUND BRAIN TISSUE SCANNING. THE STATEMENTS FIRST CONSIDER ROBOTIC SCANNING IN GENERAL, THEN COMPARE ROBOTIC TO MANUAL SCANNING ACROSS FIVE CATEGORIES.

Statements: The robot …	**Assessment**
…approaches the tissue carefully and safely.	Agree
…performs smooth and controlled probe motions.	Somewhat agree
…does not behave unexpectedly.	Somewhat agree
…interacts gently with the tissue, without exposing it to too high interaction forces, and thus avoids unnecessary tissue deformations.	Agree
…reliably aligns the probe perpendicular to the tissue surface in the beginning.	Agree
…reacts appropriately to acoustic shadow in the image by adapting the probe pose to improve probe-tissue coupling.	Agree
…performs a fan motion that covers an appropriate volume of brain tissue.	Agree
…is capable of performing a fan motion in two perpendicular planes, e.g., the coronal and sagittal plane.	Agree
…records ultrasound images of high diagnostic quality.	Agree
Categories: The robot achieves …compared to manual scanning.	**Assessment**
Diagnostic quality of acquired ultrasound images (**Better** = higher quality data)	Equivalent
Gentility of probe-tissue interaction (**Better** = more gentle and soft interaction)	Equivalent
Stability of probe-tissue coupling (**Better** = more stable, less breaking of contact)	Slightly better
Smoothness of probe motions (**Better** = smoother motion with more constant velocity)	Slightly better
Perceived safety of tissue scanning (**Better** = safer scanning)	Equivalent

Extended Data B
Caption for Movie E1.

Video showing the robotic ultrasound scanning system and *ultrasonic servoing* control method in action. The video directly mirrors some data figures of the manuscript, allowing readers to track the robot motions generating the plots. It contains an overview of the system setup with the corresponding manuscript Figure 8. Further, the video shows recordings of robotic and manual ultrasound scanning protocol executions on ex-vivo porcine brain, synchronized with the corresponding ultrasound images and animated versions of Figures 2,3 and 7.

Extended Data C
Caption for Data E1.

Excel file containing underlying data of all plots of the main manuscript. Each sheet within the file contains the data used to plot results shown in the Figure panels Fig. 2e-h, Fig. 3b-e, Fig. 4a-e, Fig. 6, Fig. 7b-d. Units of each column are the same as used in the plots of the manuscript.

Supplementary Information for

Ultrasonic servoing for autonomous intraoperative robotic imaging in neurosurgery: ex-vivo experiments and medical assessment

Michael Dyck[1,2*], Arne Sachtler[2,1], Luke Dixon[3], Alexander Kirst[1], Bernhard Weber[1], Alistair Weld[4], Sophie Camp[5], Stamatia Giannarou[4,6], Alexander Dietrich[1], Julian Klodmann[1=], and Alin Albu-Schäffer[1,2=]

[*]Corresponding author. Email: michael.dyck@dlr.de

[1]German Aerospace Center (DLR), Institute of Robotics and Mechatronics, 82234 Wessling, Germany.

[2]Technical University of Munich, Department of Computer Engineering, 85748 Garching, Germany.

[3]Imperial College London, Faculty of Medicine, Division of Surgery and Cancer, and Imperial College Healthcare NHS Trust, Department of Neuroradiology, London, UK.

[4]Imperial College London, The Hamlyn Centre, London SW7 2AZ, UK.

[5]Imperial College London, Faculty of Medicine, Division of Surgery and Cancer, and Imperial College Healthcare NHS Trust, Department of Neurosurgery, London, UK.

[6]Imperial College London, Faculty of Medicine, Department of Surgery and Cancer, London SW7 2AZ, UK.

[=]These authors contributed equally.

This supplementary information shows two experimental setups in Supplementary A to additionally demonstrate the approach of this work on tissue phantoms rather than ex-vivo brain. Further, it presents in more detail the methods presented in this work in Supplementary B. This includes the ultrasonic servoing control cascade, addressing the question of how to land the ultrasound probe onto the unknown tissue, achieving perpendicular probe alignment and maintaining contact while avoiding acoustic shadowing artifacts and minimizing the interaction forces.

SUPPLEMENTARY A
PHANTOM EXPERIMENTS

Fig. S1 shows two experimental setups to additionally demonstrate the approach of this work on tissue phantoms rather than ex-vivo brain. Notation and a summary of all methods used here is explained in the main manuscript and Supplementary B. The two different ultrasound probes and tissue phantoms used in each of the experiments are presented in Figs. S1c and S1d. The UKF parameters common for all following experiments are summarized in Table S1. Initial values for the state covariance are set based on heuristically chosen values for the maximum feasible state change per Unscented Kalman Filter (UKF) iteration, that ensure smooth and slow filter convergence $\Delta \boldsymbol{p}_{max} = \begin{pmatrix} 0.001\,\mathrm{m} & 0.1\,{}^{1}\!/_{\mathrm{m}} & 0.5\,^\circ & 0.5\,^\circ \end{pmatrix}$, keeping in mind also the expected spread of the sigma points. To identify the measurement noise we performed several manual experiments, statically recording ultrasound images on different positions on the phantom, and calculating the resulting standard deviation of c and s. To be more robust against measurement noise and outliers, we specify $\sigma_{r_c}, \sigma_{r_s}$ in Table S1 conservatively, being about twice as high as the values identified manually. We set the gains for the PI controller (S37) to $k_p = 10^{-3}$ and $k_i = 10^{-5}$.

A. Linear ultrasound probe and custom-made phantom

For the first experiments, we use the lightweight, torque-controlled, seven degrees of freedom (DoF) robot arm DLR MIRO [S1] and attach a *GE 12L-RS* linear ultrasound probe via a 3D printed mechanical interface, connected to a *GE LOGIQ e* ultrasound machine. The transformation from the robot's TCP to the tip of the ultrasound probe $\boldsymbol{x}_t$ is known from CAD design. Torque sensing in all seven joints allows to directly command joint torques calculated by the impedance controller (6). For evaluation, a six DoF *ATI Mini45 Titanium* force/torque sensor between ultrasound probe and robot flange measures interaction forces during scanning. We implement the individual components of the ultrasonic servoing controller in C++, build the closed-loop system in MATLAB/Simulink and execute it on a real-time computing host. The DLR MIRO is controlled at a rate of $3\,$kHz, while the ultrasound system provides data at $60\,$Hz.

TABLE S1
UKF PARAMETERS, STIFFNESSES AND OTHER PARAMETERS FOR ALL EXPERIMENTS

	$\sigma_{\delta,0}$	$\sigma_{\kappa,0}$	$\sigma_{\theta,0}$	$\sigma_{\varphi,0}$	η_1	η_2	η_3
unit	m	1/m	deg	deg	-	-	-
	0.0005	0.05	0.2	0.2	1	0	3
	σ_{w_δ}	σ_{w_κ}	σ_{w_θ}	σ_{w_φ}	σ_{r_c}	σ_{r_s}	
unit	m	1/m	deg	deg	-	-	
	$\frac{\sigma_{\delta,0}}{100}$	$\frac{\sigma_{\kappa,0}}{10}$	$\frac{\sigma_{\theta,0}}{10}$	$\frac{\sigma_{\varphi,0}}{10}$	0.05	0.1	
	$\boldsymbol{k}_u$	k_d	$\boldsymbol{k}_\epsilon$	ζ	w	l	κ_p
unit	N/m	N/m	Nm/rad	-	-	m	1/m
A-A	2000	500	400	0.7	502	0.044	0
A-B	1000	500	100	0.7	800	0.032	29.4

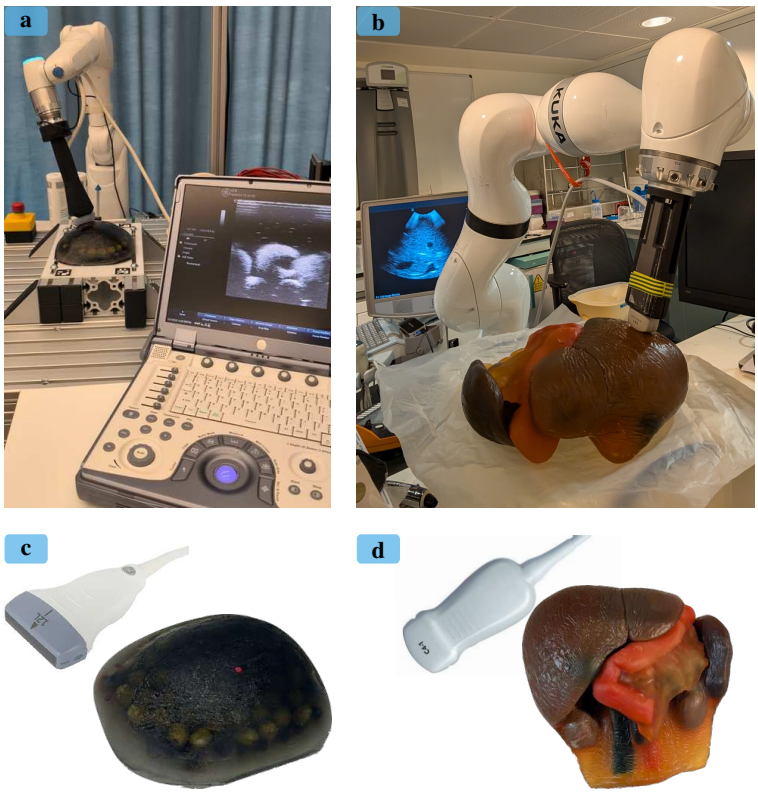

Fig. S1. **Hardware setup for phantom experiments.** The figure shows the ultrasound probe and tissue phantom used in the experiments **(a),(c)** (Supplementary A-A, DLR MIRO, linear probe, custom-made phantom), and **(b),(d)** (Supplementary A-B, KUKA LBR iiwa, convex probe, laparoscopic phantom).

Depending on the extent of visible tissue in an ultrasound image, the acoustic shadow detection algorithm, and the UKF, run at 5-10 Hz, while the PI controller (S37) runs at 100 Hz.

A custom-made phantom based on GELITA® GELATINE *Type Ballistic 3* simulates organ tissue for intraoperative ultrasound scanning. Adding glycerine increases durability of the phantom, and adjusting the water to gelatin ratio allows mimicking tissues of various stiffnesses. Inspired by [S2], different objects (olives, blueberries and flour) placed randomly into the phantom replicate the echogenic appearance and inhomogeneity of real tissue. In this experiment, we created a phantom with a water/glycerine/gelatin ratio of 19/19/2 by pouring the dissolved, preheated mixture into the negative of a custom-made convex surface of varying curvature. We use the geometry of this convex surface to evaluate the experimental performance of the ultrasonic servoing controller.

Controller stiffnesses and other parameters for this set of experiments are summarized in Table S1.

1) Acoustic coupling and interaction force: We performed two experiments, initializing the robot at the same position above an arbitrarily chosen point on the phantom and following the workflow presented in the main manuscript, Methods, section *Ultrasonic servoing control*. Results are depicted in Fig. S2, the corresponding UKF (expected) measurements are shown in Fig. S3. The two experiments differ only in the specification of $\hat{c}_{\text{des}} = 0.85$ (Figs. S2a, S3a) and $\hat{c}_{\text{des}} = 0.50$ (Figs. S2b, S3b). In Fig. S2, the first row depicts the estimated curvature $\hat{\kappa}$ alongside the rotational trajectory in β in the range of $\beta \in [-90°, 90°]$. The second row highlights the desired and actual distance $d_{u,\text{des}}, \hat{d}_u$ between ultrasound probe and estimated tissue surface, with $d_{u,\text{des}}$ calculated according to (S37) for $\hat{c}_{\text{des}} = 0.85$ and $\hat{c}_{\text{des}} = 0.5$ in left and right column, respectively. The interaction force in direction of the probe's longitudinal axis $\tilde{\boldsymbol{z}}$ measured with the dedicated force/torque sensor is visualized in the third row. Lastly, Fig. S2 shows at some exemplary points in time the ultrasound image and corresponding acoustic coupling $\boldsymbol{a}$ to illustrate the coupling performance.

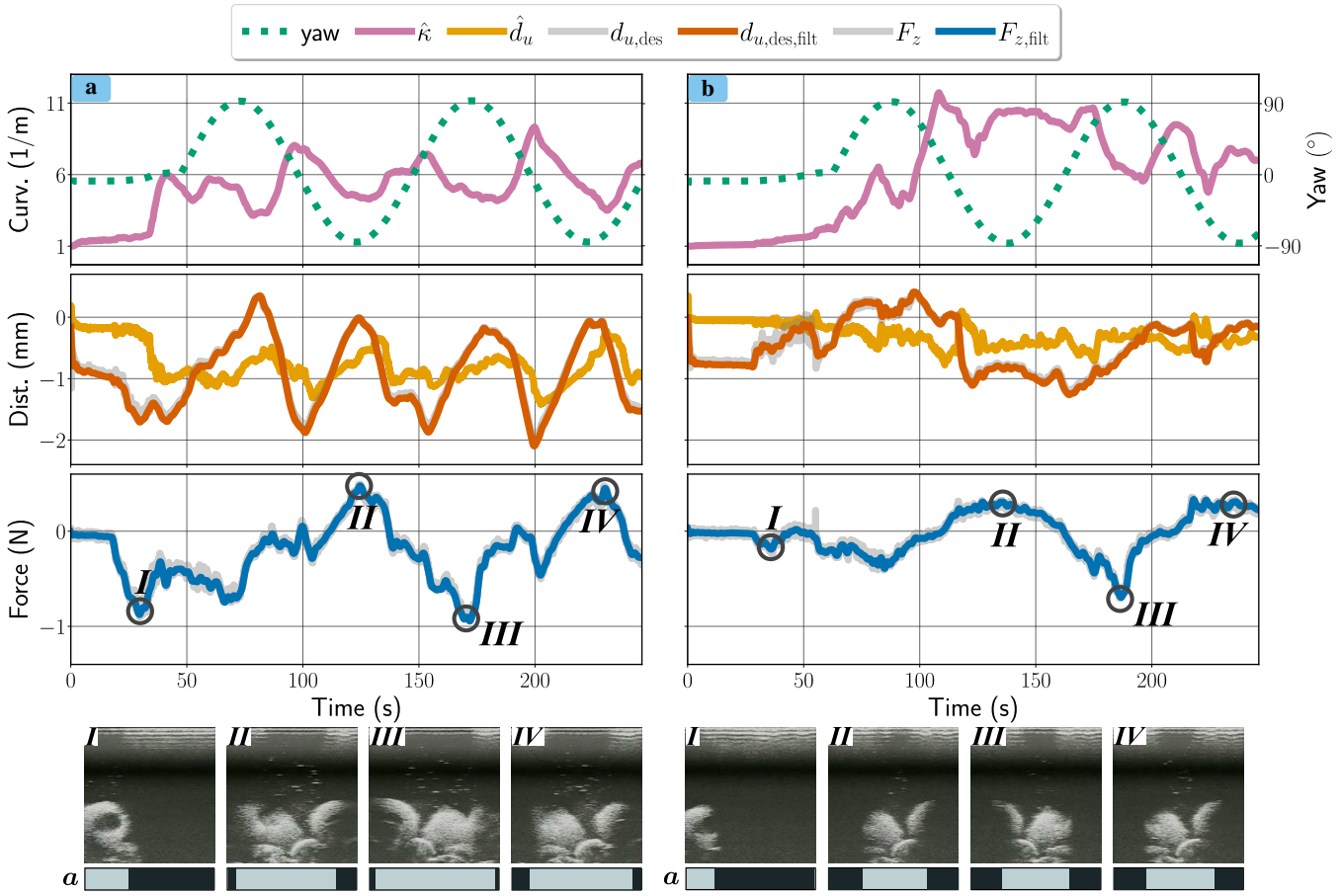

Fig. S2. **Results for the experiments Supplementary A-A1.** Plots show the probe landing on the same point on the tissue phantom surface for $\hat{c}_{\mathrm{des}} = 0.85$ (**a**) and $\hat{c}_{\mathrm{des}} = 0.50$ (**b**). Estimated curvature $\hat{\kappa}$ of and distance $\hat{d}_u$ to $\mathcal{S}_u$, desired distance $d_{u,\mathrm{des}}$ to realize a given $\hat{c}_{\mathrm{des}}$, and probe yaw rotation are mainly responsible for fluctuations in the interaction force F_z. Sample ultrasound images (***I*** - ***IV***) and the corresponding acoustic coupling $\boldsymbol{a}$ show proper coupling.

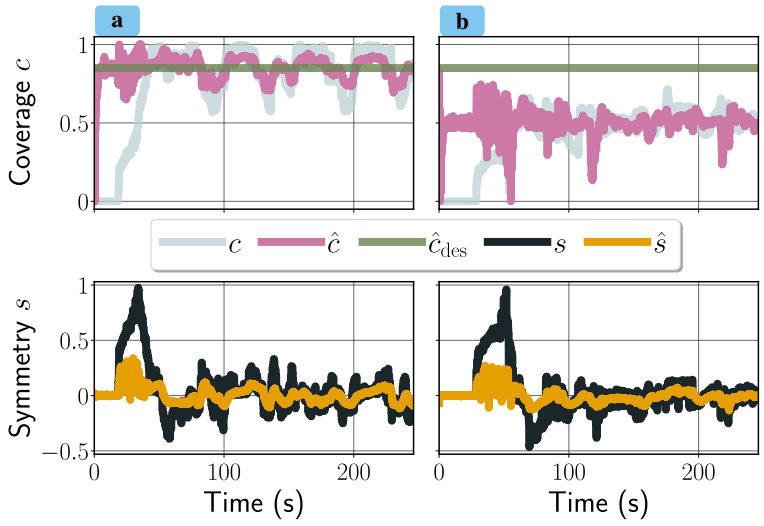

Fig. S3. **UKF measurements (c, s) and expected measurements $(\hat{c}, \hat{s})$.** Values correspond to the two experiments shown in Fig. S2 (cf. Supplementary A-A1). The two experiments differ in the value for $\hat{c}_{\mathrm{des}} = 0.85$ (**a**) and $\hat{c}_{\mathrm{des}} = 0.50$ (**b**).

The probe approaches the surface and establishes contact at around $t \approx 15\,\mathrm{s}$ and $t \approx 30\,\mathrm{s}$ for both experiments, respectively. Contact establishment is indicated by a non-zero interaction force and non-zero measurements $\boldsymbol{z}$. Right after establishing contact (cf. $\boldsymbol{I}$ in Fig. S2), the probe is oriented quickly to achieve a symmetric distribution of $\boldsymbol{a}$ across the ultrasound image, equivalent to realizing $s \approx 0$ as can be seen in the second row of Fig. S3 (remember objective $\mathrm{O}_{2.1}$). This is realized for any rotational angle β as demanded with objective $\mathrm{O}_{2.2}$, resulting in the probe aligned normal to the unknown tissue surface. Quantitatively, this is reflected in the mean value for s in both experiments (after probe alignment in the initial plane Γ, i.e., when the rotation in β starts) being $\bar{s} = 0.047$ and $\bar{s} = 0.024$, respectively.

The extent of acoustic coupling and the correlating interaction force with the tissue is dominantly influenced by the value specified for $\hat{c}_{\mathrm{des}}$. Mean interaction forces for both experiments, again taken after the initial probe alignment, as soon as the probe rotation initiates, are $\bar{F}_z = -0.197\,\mathrm{N}$ and $\bar{F}_z = -0.013\,\mathrm{N}$, respectively. Fluctuations in the measured interaction force mainly stem from changes in the estimated curvature $\hat{\kappa}$, and correspondingly changes in the distance necessary to achieve a certain c, as highlighted in the first two columns of Fig. S2. The first row in Fig. S3 confirms that, with mean values for c of $\bar{c} = 0.750 \approx \hat{c}_{\mathrm{des}} = 0.85$ and $\bar{c} = 0.420 \approx \hat{c}_{\mathrm{des}} = 0.5$. The sample ultrasound data show accurate realization of the desired coverage, where, e.g., a $\hat{c}_{\mathrm{des}} = 0.5$ results in approximately $50\ \%$ of the image showing visible tissue.

2) Local surface reconstruction: It remains to show the local surface reconstruction capabilities of the presented controller, as introduced in objective O_3. Results are shown in Fig. S4. The results in Fig. S4a come from the same experiment as was used in Fig. S2b and Fig. S3b. Fig. S4b visualizes the reconstruction performance for landing the probe on another spot on the phantom.

Both figures show the true and estimated states $\boldsymbol{p}$ and $\hat{\boldsymbol{p}}$, together with the square root of the diagonal entries of the state covariance matrix $\boldsymbol{P}_k$ as lightblue shading. The larger this lightblue area, the higher the state uncertainty at that point in time. Overall, the UKF shows good reconstruction of the local surface geometry. The second row of Fig. S4 additionally depicts the polar and azimuthal angle $\theta_{\tilde{z}}$ and $\varphi_{\tilde{z}}$ of the z-axis $\tilde{\boldsymbol{z}}$ of the ultrasound probe. With the state estimates $\hat{\theta}, \hat{\varphi}$ converging to the real solution and the ultrasound probe orientation following these estimates, i.e., $\theta_{\tilde{z}} \approx \hat{\theta}$ and $\varphi_{\tilde{z}} \approx \hat{\varphi}$, the probe is aligned normal to the tissue surface. The last row of Fig. S4 presents a zoomed in view on the trajectory of the two spherical angles of the state vector, together with the rotational trajectory around the probe's longitudinal axis. Here, the relation between β and the UKF's uncertainty on θ and φ becomes visible. Times with low

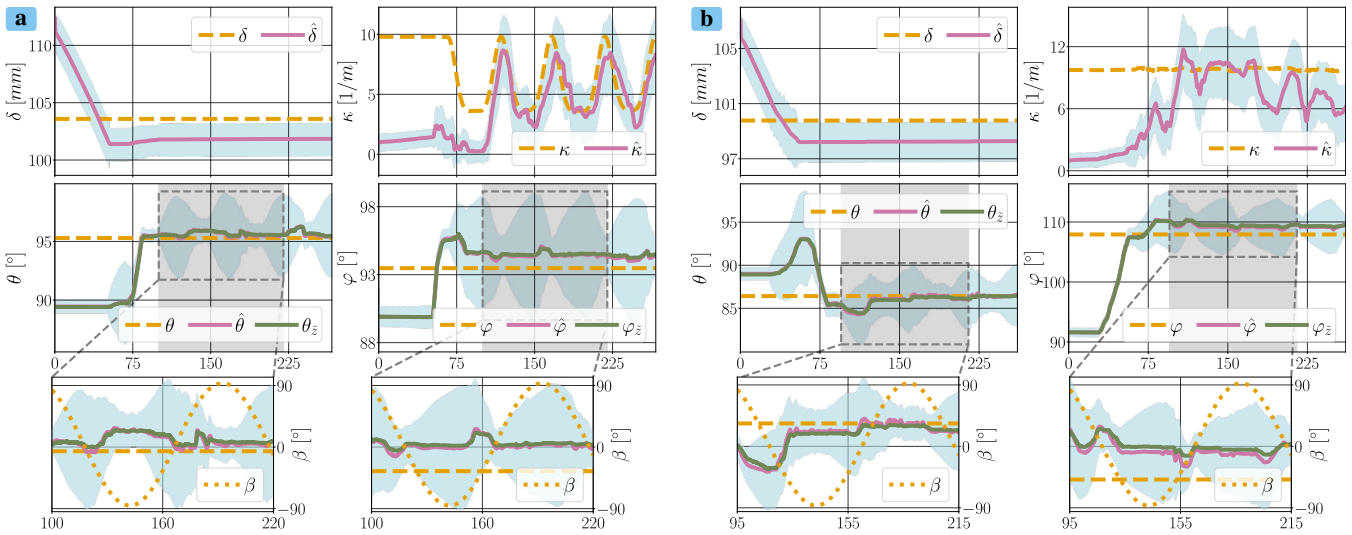

Fig. S4. **Performance evaluation of local surface reconstruction.** Plots show the convergence of the UKF estimated states $\hat{\boldsymbol{p}}$ to the true states $\boldsymbol{p}$ (cf. Supplementary A-A2) for two distinct points on the phantom (panels (**a** and **b**)). The green lines represent the polar ($\theta_{\tilde{z}}$) and azimuthal ($\varphi_{\tilde{z}}$) angle of the probe's z-axis. State uncertainty is visualized as light blue shading. The lower row shows a zoom-in view on the trajectory above, including the rotational yaw trajectory in β.

uncertainty in one of the angles correspond to high uncertainty in the other, and vice versa. This stems from the fact that the measurement $\boldsymbol{z}$ can only provide information on the probe's in-plane orientation. The uncertainty in κ does not decrease over time, as the UKF has to constantly adjust its state estimate $\hat{\kappa}$ to compensate for the probe rotation.

The remaining part is the curvature tensor according to objective $O_{3.3}$. We keep track of the minimum and maximum curvature values during operation, but these will be noisy and no good estimates of the curvature tensor. Instead, we take the full history of estimated normal curvature and fit the parameters of a curvature tensor. As in (S2), let the angle α describe the orientation in the tangent plane relative to the maximum principal curvature. Neither the principal curvature directions nor their values are known, but we know it is a fixed offset β_0 from the probe's yaw orientation β. Let $\alpha = \beta - \beta_0$:

$$\kappa(\beta) = \kappa_1 \cos^2(\beta - \beta_0) + \kappa_2 \sin^2(\beta - \beta_0), \tag{S1}$$

for some unknown offset angle β_0. We formulate this as least squares problem. Take the history β_i and $\hat{\kappa}_i$ for T samples. Then,

$$L = \sum_{i=1}^{T} \left(\kappa_1 \cos^2(\beta_i - \beta_0) + \kappa_2 \sin^2(\beta_i - \beta_0) - \hat{\kappa}_i \right)^2,$$

where, $\hat{\kappa}_i$ denotes the estimated curvature at time t_i and β_i the yaw angle of the probe at the same time. We numerically solve this nonlinear least squares problem using the Trust Region Reflective algorithm [S3] and obtain $\beta_0, \kappa_1, \kappa_2 = \arg\min L(\beta_0, \kappa_1, \kappa_2)$.

Fig. S5 shows experimental results for the same experiments as before (cf. Fig. S4). The polar plots show curvature values on the radial axis over the ultrasound probe's longitudinal orientation β. The surface is curved differently at the two contact points (dashed lines in Fig. S5). We compute those curvature profiles on triangle mesh models of our surfaces using `libigl` [S4]. Solid orange lines show the history of the estimated normal curvature $\hat{\kappa}_i$ over β_i, and the blue solid line represents the curvature profile based on the fitted curvature tensor.

B. Convex ultrasound probe and laparoscopic phantom

To show the generic applicability of all components of the ultrasonic servoing controller, we perform one additional experiment using a different ultrasound machine and probe, a commercially available tissue phantom, and a different robotic manipulator. Fig. S1d shows the corresponding experimental setup. Here, we deploy the seven DoF *KUKA LBR iiwa* robot arm holding a *Zonare C4-1* convex ultrasound probe, connected to a *Zonare Z.One PRO* ultrasound machine. The commercially available *Abdominal Intraoperative & Laparoscopic Ultrasound Phantom "IOUSFAN"* by *Kyoto Kagaku Co.* serves as soft-tissue phantom. As was the case for the experiments in Supplementary A-A, the ultrasound system provides data at 60 Hz, while the UKF operates at 5-10 Hz. The KUKA robot arm is controlled at a rate of 1 kHz, the PI controller (S37) is again running at 100 Hz. Table S1 lists the controller stiffnesses and remaining parameters for this experiment.

We perform one experiment equivalent to those in Supplementary A-A, landing the convex ultrasound probe onto a randomly chosen point on the liver of the IOUSFAN phantom, and initiating probe rotation after UKF convergence in the initial plane. This time, we specify $\hat{c}_{\text{des}} = 0.75$. Results are depicted in Fig. S6, showing the estimated curvature, the ultrasound probe rotational trajectory, estimated and desired distance to the unknown tissue phantom surface, and true and expected measurements. Contact establishment happens at $t \approx 15$ s, probe rotation initiates shortly after. The first and second row of Fig. S6 highlight once more the strong influence of the surface's estimated normal curvature on the distance set point for the surface impedance controller. Some sample ultrasound images, now being of convex shape, taken during the experiment show good acoustic coupling. This also reflects in the mean value of $\bar{c} = 0.759 \approx \hat{c}_{\text{des}}$. Furthermore, $\bar{s} = 0.073 \approx 0$ for all values of β throughout the scanning again indicates perpendicular probe alignment.

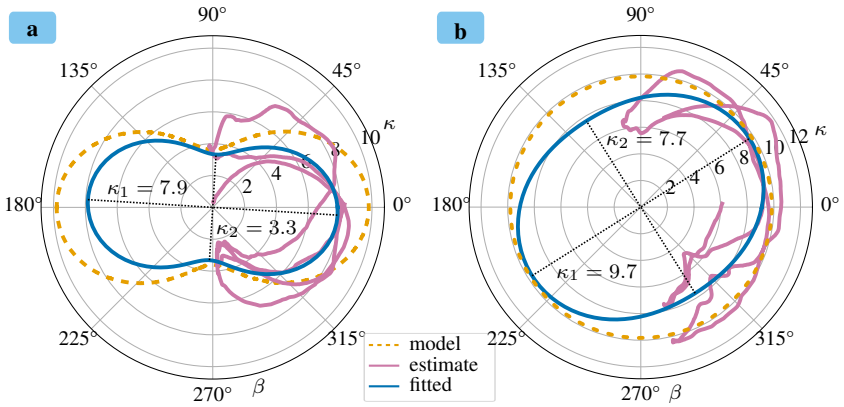

Fig. S5. **Fitted curvature tensor following** (S1)**.** The panels (**a**) and (**b**) correspond to those in Fig. S4. The polar plots show the relation of curvature κ and yaw angle β.

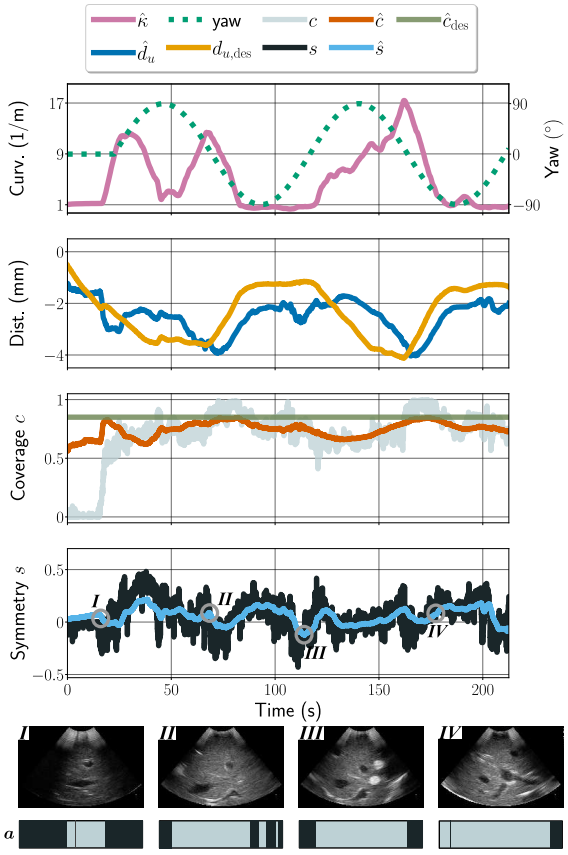

Fig. S6. **Results of the experiment Supplementary A-B.** As opposed to Supplementary A-A, convex ultrasound images are evaluated for acoustic shadow. The desired extent of contact is $\hat{c}_{\mathrm{des}} = 0.75$.

We refrain from showing the state values in this experiment as done in Fig. S4, since no ground truth of the surface geometry of the IOUSFAN phantom was available. Still, the recorded measurements indicate convergence to the true states θ, φ. Qualitatively, also the estimated curvature $\hat{\kappa}$ depicted in Fig. S6, and correspondingly the state estimate $\hat{\delta}$, seem reasonable, as the probe was landed on the liver at a point with relatively high and low principal curvature values, respectively.

SUPPLEMENTARY B
METHODS

Going into more detail, let $\mathcal{S}_u \subset \mathbb{R}^3$ be an unknown two-dimensional surface modeling the scanned tissue, and let $\boldsymbol{\psi} \in \mathcal{S}_u$ be any desired target point of contact with the ultrasound probe. With this, we refine the high level objective O_3 of the main manuscript to be:

(O_3) Approximation of the local geometry of $\mathcal{S}_u$ around $\boldsymbol{\psi}$, i.e., identification of

- ($O_{3.1}$) the position of $\boldsymbol{\psi} \in \mathcal{S}_u \subset \mathbb{R}^3$;
- ($O_{3.2}$) the unit normal vector $\boldsymbol{n}_u(\boldsymbol{\psi})$ at $\boldsymbol{\psi}$;
- ($O_{3.3}$) the curvature tensor of $\mathcal{S}_u$ at $\boldsymbol{\psi}$.

Furthermore, given the length l of the ultrasound probe, i.e., the length of the line along which the individual transducer elements are distributed, we assume that

(A_1) the curvature of $\mathcal{S}_u$ in a circular neighborhood of radius $l/2$ around $\boldsymbol{\psi}$ is symmetric.

A. *Curvature Tensor*

We briefly recap the concept of (normal) curvature and the curvature tensor, needed for objective $O_{3.3}$. Consider Fig. S7a for visualizations. For a deeper introduction we recommend [S5].

Consider a point $\boldsymbol{\psi}$ on $\mathcal{S}_u$ and take an arbitrary tangent direction $\boldsymbol{X} \in \mathcal{T}_{\boldsymbol{\psi}}\mathcal{S}_u$. Intersect the surface with the plane spanned by $\boldsymbol{X}$ and the surface normal $\boldsymbol{n}(\boldsymbol{\psi})$. Locally at $\boldsymbol{\psi}$, the resulting planar curve can be described by an osculating circle, a circle of radius $r = 1/\kappa$ that best approximates the curve around $\boldsymbol{\psi}$. Here, $\kappa(\boldsymbol{X})$ is the normal curvature of $\mathcal{S}_u$ at $\boldsymbol{\psi}$ in the direction $\boldsymbol{X}$. The maximum $\kappa_1 = \max_X \kappa(\boldsymbol{X})$ and minimum $\kappa_2 = \min_X \kappa(\boldsymbol{X})$ values are called principal curvatures κ_1, κ_2 and their respective directions principal curvature directions $\boldsymbol{X}_1, \boldsymbol{X}_2$. Note that there are no unique principal curvature directions for planar (curvature-free, $\kappa_1 = \kappa_2 = 0$) or umbilical (sphere-like, $\kappa_1 = \kappa_2$) points. Principal curvature directions are always perpendicular.

Euler's Curvature Formula [S5] states that the normal curvature κ in a tangent direction $\boldsymbol{X}$ given by its angle α relative to $\boldsymbol{X}_1$ is

$$\kappa(\alpha) = \kappa_1 \cos^2(\alpha) + \kappa_2 \sin^2(\alpha). \tag{S2}$$

When varying α, the normal curvature (S2) oscillates sinusoidally between the principal curvature values κ_1 ($\alpha = 0$) and κ_2 ($\alpha = \pi/2$). We follow the sign convention of a positive curvature meaning the surface is bending away from its normal, i.e., being locally convex.

The magnitude of the normal curvature has a strong influence on how the ultrasound probe has to interact with the tissue to achieve acoustic coupling in the sense of maintaining a certain $\boldsymbol{a}^w$. As can

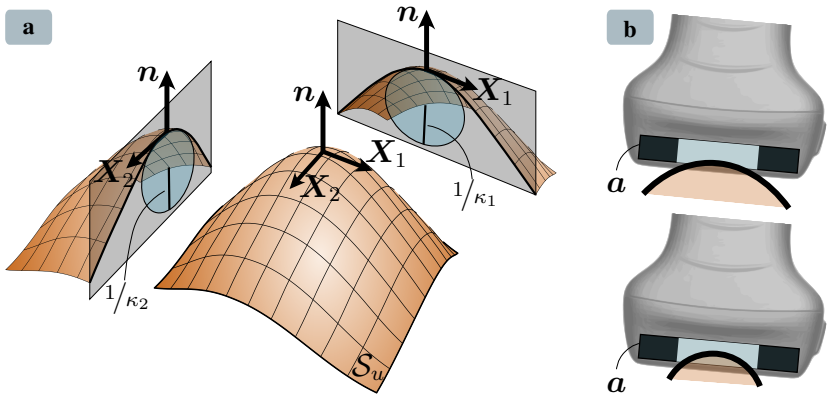

Fig. S7. **Curvature of surfaces. (a)** Principal curvature directions $\boldsymbol{X}_1, \boldsymbol{X}_2$ are those where the surface bends the most / least. The curvatures are called principal curvature values κ_1, κ_2. **(b)** The higher the normal curvature, the more the ultrasound probe needs to penetrate into the tissue to maintain the same acoustic coupling $\boldsymbol{a}$, assuming the same stiffness in all cases.

be seen in Fig. S7b, a higher normal curvature, i.e., a smaller radius for the osculating circle, requires the probe to penetrate deeper into the tissue. A higher normal curvature, i.e., a smaller radius for the osculating circle, requires the probe to penetrate deeper into the tissue.

B. Surface-centric Impedance Control

We recap details of the surface-centric impedance control [S6] that allows to control a tool relative to an arbitrary surface $\mathcal{S} \subset \mathbb{R}^3$. Let $\boldsymbol{x}_t = \begin{pmatrix} x_t & y_t & z_t \end{pmatrix}^\mathsf{T} \in \mathbb{R}^3$ be the translational component of the Cartesian forward kinematics $f_{\text{kin}} : \mathcal{Q} \to SE(3) \mid \boldsymbol{q} \mapsto \boldsymbol{x} = f_{\text{kin}}(\boldsymbol{q})$, where $\boldsymbol{q} \in \mathcal{Q}$ represent generalized configuration coordinates of the robotic manipulator. In other words, $\boldsymbol{x} \in SE(3)$ describes the pose of the ultrasound probe. The impedance controller [S6] realizes a virtual spring-damper system acting in surface-centric task coordinates (cf. Fig. S8)

$$\boldsymbol{\rho} = \begin{pmatrix} u_1(\boldsymbol{q}) \\ u_2(\boldsymbol{q}) \\ d(\boldsymbol{q}) \\ \boldsymbol{\epsilon}(\boldsymbol{q}) \end{pmatrix}, \tag{S3}$$

where u_1, u_2 are coordinates on the surface $\mathcal{S}$, d is the signed distance between the ultrasound probe and the surface, and $\boldsymbol{\epsilon}$ describes the orientational deviation from the surface normal. With the task coordinates (S3) we implement an impedance control law [S7, S8]

$$\boldsymbol{\tau} = \boldsymbol{J}_\rho^\mathsf{T}(\boldsymbol{q})[\boldsymbol{K}_\rho(\boldsymbol{\rho}_{\text{des}} - \boldsymbol{\rho}(\boldsymbol{q})) + \boldsymbol{D}_\rho(\boldsymbol{q})(\dot{\boldsymbol{\rho}}_{\text{des}} - \boldsymbol{J}_\rho(\boldsymbol{q})\dot{\boldsymbol{q}})], \tag{S4}$$

with $\boldsymbol{\tau} \in \mathbb{R}^n$ being the desired joint torques of an n-DoF, torque-controlled manipulator. $\boldsymbol{J}_\rho(\boldsymbol{q}) \in \mathbb{R}^{6\times n}$ denotes the Jacobian of $\boldsymbol{\rho}(\boldsymbol{q})$, i.e., the product $\boldsymbol{J}_\rho = \boldsymbol{J}_{\rho x}\boldsymbol{J}_x$ of the known geometrical Jacobian $\dot{\boldsymbol{x}} = \begin{bmatrix} \boldsymbol{v} & \boldsymbol{\omega} \end{bmatrix}^\mathsf{T} = \boldsymbol{J}_x(\boldsymbol{q})\dot{\boldsymbol{q}}$ and the Jacobian of $\boldsymbol{\rho}(\boldsymbol{x})$.

The surface-centric task coordinates (S3) are calculated by finding the proxy point $\boldsymbol{\chi} \in \mathcal{S}$ closest to $\boldsymbol{x}_t$. Then, $\boldsymbol{u}(\boldsymbol{\chi}) \in \mathcal{X}$ are the coordinates of this proxy point in the parameter domain $\mathcal{X} \subset \mathbb{R}^2$. $\mathcal{X}$ results from the inverse of a parametrization $\Phi : \mathcal{X} \to \mathcal{S}$. $d(\boldsymbol{q})$ represents the signed distance between ultrasound probe and proxy point. The remaining coordinates $\boldsymbol{\epsilon}(\boldsymbol{q}) \in \mathbb{R}^{3\times 1}$ are the vector part of the unit quaternion $\boldsymbol{h} = [\lambda, \boldsymbol{\epsilon}]$ describing the deviation of the ultrasound probe orientation to the normal vector $\boldsymbol{n}(\boldsymbol{\chi})$. We implement the impedance control law (S4) in these coordinates, with $\boldsymbol{K}, \boldsymbol{D}(\boldsymbol{q}) \in \mathbb{R}^{6\times 6}$ being the

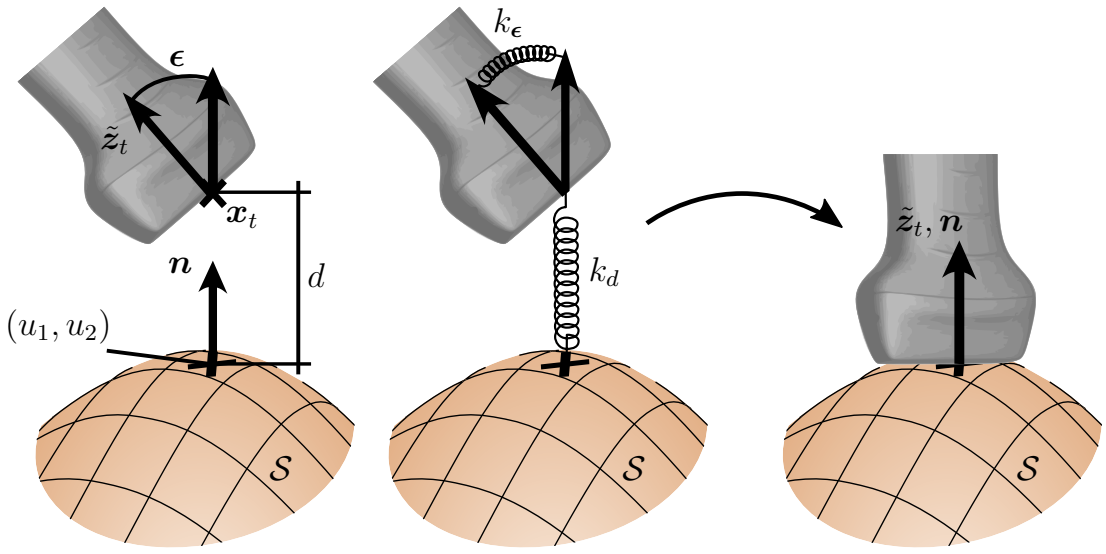

Fig. S8. **Task coordinates** (S3) **of the surface-centric impedance controller.** A virtual mass damper system pulls the ultrasound probe ($\boldsymbol{x}_t$) towards a point (u_1, u_2) on the surface $\mathcal{S}$ and aligns the probe's z-axis $\tilde{\boldsymbol{z}}_t$ with the surface normal $\boldsymbol{n}$.

symmetric, positive definite stiffness and damping matrices, respectively, where $\boldsymbol{K} = \mathrm{diag}\begin{pmatrix}\boldsymbol{k}_u & k_d & \boldsymbol{k}_\epsilon\end{pmatrix}$. $\boldsymbol{D}(\boldsymbol{q})$ is designed based on the damping coefficient $\zeta \in \mathbb{R}$ and double diagonalization design proposed in [S9]. The Jacobian of $\boldsymbol{\rho}(\boldsymbol{x})$ is

$$\boldsymbol{J}_{\rho x} = \frac{\partial \boldsymbol{\rho}(\boldsymbol{x})}{\partial \boldsymbol{x}} = \begin{bmatrix} \boldsymbol{J}_{uv} & \boldsymbol{0}_{2\times 3} \\ \boldsymbol{J}_{dv} & \boldsymbol{0}_{1\times 3} \\ \boldsymbol{J}_{\epsilon v} & \boldsymbol{J}_{\epsilon\omega} \end{bmatrix} \in \mathbb{R}^{6\times 6}, \tag{S5}$$

with $\boldsymbol{v}$ and $\boldsymbol{\omega}$ denoting the translational and angular velocity vectors, respectively.

For brevity, we omit equations for the components $\boldsymbol{J}_{dv} \in \mathbb{R}^{1\times 3}$ – describing the linear relation between $\boldsymbol{v}$ and velocity in the distance coordinate $\dot{d}$ – and $\boldsymbol{J}_{\epsilon\omega} \in \mathbb{R}^{3\times 3}$ – representing the mapping from angular velocities $\boldsymbol{\omega}$ of the end-effector onto velocities in $\boldsymbol{\epsilon}$ (cf. [S6] for details). $\boldsymbol{J}_{uv}$ relates $\boldsymbol{v}$ to velocities in the parametrization coordinates $\boldsymbol{u}(\boldsymbol{\chi}) \in \mathcal{X}$. Calculation of this term depends upon the gradient vectors $\nabla u_1, \nabla u_2$, i.e., the directional derivatives of $\boldsymbol{u}$ for any vector tangent to the surface. Lastly, the derivation of $\boldsymbol{J}_{\epsilon v}$ requires basic concepts from differential geometry, we recommend [S5] for a visual introduction to the topic. More in-depth derivations can be found in [S6]. $\boldsymbol{J}_{\epsilon v}$ relates translational velocities $\boldsymbol{v}$ to $\dot{\boldsymbol{\epsilon}}$, stemming from the fact that any motion of the proxy point $\boldsymbol{\chi} \in \mathcal{S}$ in a tangent direction $\boldsymbol{X} \in \mathcal{T}_\chi \mathcal{S}$ changes the corresponding surface normal $\boldsymbol{n}(\boldsymbol{\chi})$ whenever the normal curvature κ_n in said direction is non-zero. The concept in differential geometry describing this relation is the *Weingarten map* [S5] $d\boldsymbol{n}(\boldsymbol{X})$. Omitting details, and using the Weingarten map and principal curvature directions $\boldsymbol{X}_1, \boldsymbol{X}_2$, we obtain

$$\boldsymbol{J}_{\epsilon v} = \boldsymbol{J}_{\epsilon\omega}[\boldsymbol{n}]_\times d\boldsymbol{n}(\boldsymbol{X}) = \boldsymbol{J}_{\epsilon\omega}[\boldsymbol{n}]_\times \boldsymbol{S}^\mathsf{T} \begin{bmatrix} \kappa_1 & 0 \\ 0 & \kappa_2 \end{bmatrix} \boldsymbol{S}, \tag{S6}$$

with $\boldsymbol{S} \in \mathbb{R}^{2\times 3}$ containing $\boldsymbol{X}_1, \boldsymbol{X}_2$ as rows, and $[\boldsymbol{n}]_\times$ denoting the skew-symmetric cross product matrix of the normal vector.

Specifying $\boldsymbol{\rho}_d \in \mathbb{R}^6$ allows controlling the position of the ultrasound probe on and its distance to the surface $\mathcal{S}$, as well as the probe orientation relative to the surface normal. Perpendicular alignment of the probe is achieved by setting $\boldsymbol{\epsilon}_d = \boldsymbol{0}$. For $d_d > 0$ the robot guides the probe along the tissue without being in contact. Establishment of contact initiates at $d_d = 0$, for direct interaction with the tissue $d_d < 0$. The resulting passive contact forces depend on the value of d_d, as well as on the controller and object stiffnesses. Continuous adaption of the desired distance from, e.g., $d_d > 0 \rightarrow d_d < 0$ enables the probe to gently approach and interact with the tissue surface.

As we assume no knowledge of the pose and geometry of the unknown target surface $\mathcal{S}_u$, we define the controller surface simply to be a planar surface positioned below the object, its normal vector aligned with the z-axis of the robot's base coordinate frame, and refer to it as base surface $\mathcal{S}_b$. Think of $\mathcal{S}_b$ representing the table carrying the tissue to be scanned. Since the surface impedance control works with discretized surfaces, we represent $\mathcal{S}_b$ as a triangle mesh. We use the notation $\cdot_b, \cdot_u$ to denote quantities related to the base and target surface $\mathcal{S}_b, \mathcal{S}_u$, respectively, as visualized in Fig. S9. Now, achieving objective O_1 requires controlling the ultrasound probe to a desired distance $d_{u,\mathrm{des}}$ to $\mathcal{S}_u$ that realizes a certain desired coverage c_{des}. Similarly, perpendicular probe alignment on $\mathcal{S}_c$ (O_2) requires $\boldsymbol{\epsilon}_u = \boldsymbol{\epsilon}_{u,\mathrm{des}} = \boldsymbol{0}$. This is only possible knowing the position of $\boldsymbol{\psi} \in \mathcal{S}_u$ and the geometry of $\mathcal{S}_u$ around $\boldsymbol{\psi}$, which is precisely why we included objective O_3 in this work.

C. Local tissue surface estimation

To accomplish objective O_3 we use an observer estimating the local tissue geometry. The surface geometry observer is based on an Unscented Kalman Filter (UKF) [S10]. The UKF's current estimate is simultaneously used as the reference normal vector for the surface-centric impedance controller [S6].

As a Kalman filter, the UKF comprises a process and measurement model. We choose the UKF over the Extended Kalman Filter (EKF), as it has proven its superior performance for state estimation in nonlinear

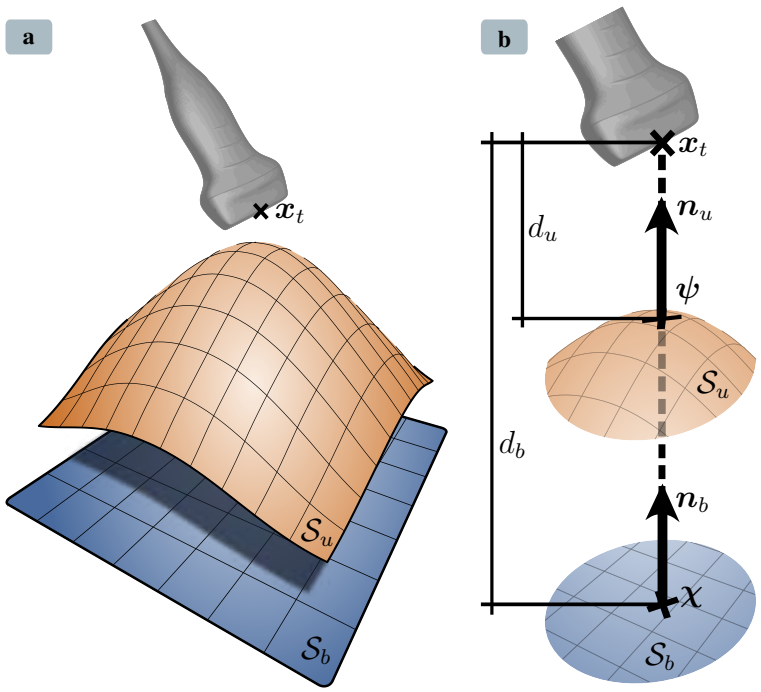

Fig. S9. **Unknown target surface and planar base surface. (a)** An ultrasound probe above the unknown target surface $\mathcal{S}_u$ and planar base surface $\mathcal{S}_b$ required for the surface impedance control. **(b)** Normal vector and distance can be defined with respect to both surfaces.

systems [S10–S12], and does not require linearization of process and measurement model, thus making it easier to implement for the given problem. We follow the notation

$$\boldsymbol{p}_k = f(\boldsymbol{p}_{k-1}, \boldsymbol{u}_{k-1}) + \boldsymbol{w}_{k-1} \tag{S7}$$
$$\boldsymbol{z}_k = h(\boldsymbol{p}_k) + \boldsymbol{v}_k. \tag{S8}$$

The process model (S7) describes how a state vector $\boldsymbol{p}_{k-1} \in \mathbb{R}^{n_p}$ at time t_{k-1} is propagated through time following a transition function f and a control input vector $\boldsymbol{u}_{k-1}$. Equation (S8) represents the measurement model, predicting the system's measurements $\boldsymbol{z}_k \in \mathbb{R}^{n_z}$ based on the estimated state $\boldsymbol{p}_k$ through the observation function h. In Kalman filtering it is assumed that, both process and measurement model, are influenced by zero-mean Gaussian noises $\boldsymbol{w}_k \sim \mathcal{N}(\boldsymbol{0}, \boldsymbol{Q}_k)$, $\boldsymbol{v}_k \sim \mathcal{N}(\boldsymbol{0}, \boldsymbol{R}_k)$ with covariances $\boldsymbol{Q}_k$, $\boldsymbol{R}_k$. Let $\boldsymbol{P}_k$ denote the current state covariance estimate. Henceforth, $\hat{\boldsymbol{p}}_k$ denotes the UKF state estimate at time t_k, as opposed to the (unknown) true state $\boldsymbol{p}_k$. We use the same notation for any quantity based on the current state estimate.

The UKF makes use of the unscented transform to approximate the distribution of a random variable propagated through a nonlinear function by again a Gaussian distribution. The posterior Gaussian is computed by generating a set of sigma points $\boldsymbol{\mathcal{P}}_i$ [S10]. Fig. S10 visualizes the idea behind the unscented transform for the example of estimating the a-priori state estimate $\hat{\boldsymbol{p}}_k^-$. In the following, we summarize the technique and UKF equations.

a) UKF equations: At each time t_k, the UKF calculates $2n_p + 1$ sigma points [S10]

$$\begin{aligned}
\boldsymbol{\mathcal{P}}_{0,k-1} &= \hat{\boldsymbol{p}}_{k-1} \\
\boldsymbol{\mathcal{P}}_{i,k-1} &= \begin{cases} \hat{\boldsymbol{p}}_{k-1} + \left(\sqrt{(n_p+\lambda)\boldsymbol{P}_{k-1}}\right)_i & i = 1 \dots n_p \\ \hat{\boldsymbol{p}}_{k-1} - \left(\sqrt{(n_p+\lambda)\boldsymbol{P}_{k-1}}\right)_{i-n_p} & i = n_p+1 \dots 2n_p \end{cases}
\end{aligned} \tag{S9}$$

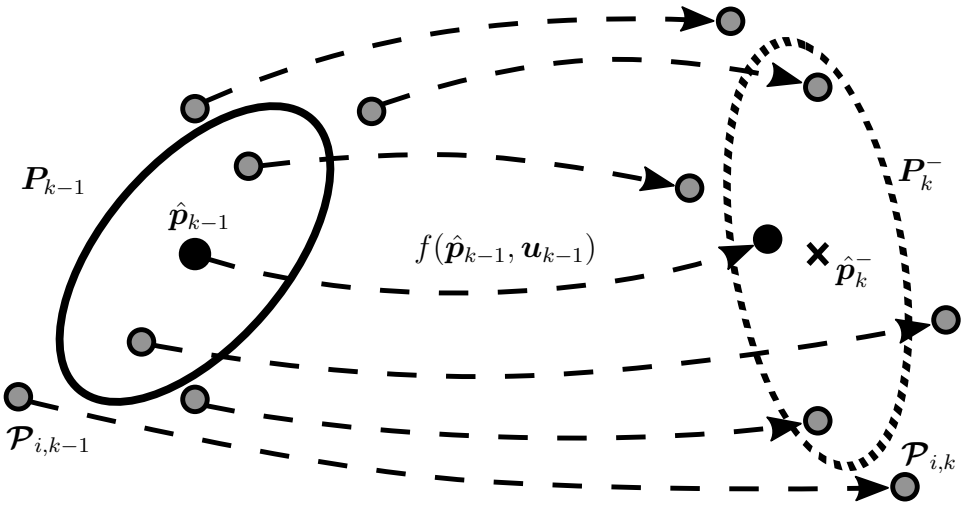

Fig. S10. **Unscented transform for the nonlinear process model** (S7)**.** The unscented transform to estimate the a-priori state estimate $\hat{\boldsymbol{p}}_k^-$ generates sigma points $\boldsymbol{\mathcal{P}}_i$, distributed around the current state estimate $\hat{\boldsymbol{p}}_{k-1}$ according to the state uncertainty $\boldsymbol{P}_{k-1}$. The process model (S7) propagates all sigma points through a transition function f using $\hat{\boldsymbol{p}}_{k-1}$ and a control input vector $\boldsymbol{u}_{k-1}$.

with $\lambda = \eta_1^2(n_p + \eta_3) - n_p$ and the i-th column of the matrix square root $\left(\sqrt{\boldsymbol{P}_{k-1}}\right)_i$. Along with (S9), a set of weights is calculated as

$$\begin{aligned} W_0^{(m)} &= \frac{\lambda}{n_p + \lambda}, \quad W_0^{(c)} = \frac{\lambda}{n_p + \lambda} + (1 - \eta_1^2 + \eta_2) \\ W_i^{(m)} &= W_i^{(c)} = \frac{1}{2(n_p + \lambda)}, \quad i = 1 \dots 2n_p. \end{aligned} \tag{S10}$$

Here, any prior knowledge of the distribution of $\boldsymbol{p}$ can be incorporated through the parameter η_2. With (S9),(S10), the UKF predicts a-priori estimates $\hat{\boldsymbol{p}}_k^-$ and $\boldsymbol{P}_k^-$ of the state and state covariance, respectively, by propagating each sigma point through the transition function f and calculating the resulting mean and covariance

$$\begin{aligned} \boldsymbol{\mathcal{P}}_{i,k} &= f(\boldsymbol{\mathcal{P}}_{i,k-1}, \boldsymbol{u}_{k-1}) \ \forall i \in [0, 2n_p] \\ \hat{\boldsymbol{p}}_k^- &= \sum_{i=0}^{2n_p} W_i^{(m)} \boldsymbol{\mathcal{P}}_{i,k} \\ \boldsymbol{P}_k^- &= \sum_{i=0}^{2n_p} W_i^{(c)} \left[\boldsymbol{\mathcal{P}}_{i,k} - \hat{\boldsymbol{p}}_k^-\right]\left[\boldsymbol{\mathcal{P}}_{i,k} - \hat{\boldsymbol{p}}_k^-\right]^\mathsf{T} + \boldsymbol{Q}_{k-1}. \end{aligned} \tag{S11}$$

In a second step, the UKF further propagates the sigma points $\boldsymbol{\mathcal{P}}_{i,k}$ through the observation function h to obtain an expected measurement $\hat{\boldsymbol{z}}_k$

$$\begin{aligned} \boldsymbol{\mathcal{Z}}_{i,k} &= h(\boldsymbol{\mathcal{P}}_{i,k}) \ \forall i \in [0, 2n_p] \\ \hat{\boldsymbol{y}}_k &= \boldsymbol{z}_k - \hat{\boldsymbol{z}}_k = \boldsymbol{z}_k - \sum_{i=0}^{2n_p} W_i^{(m)} \boldsymbol{\mathcal{Z}}_{i,k}. \end{aligned} \tag{S12}$$

The measurement residual $\hat{\boldsymbol{y}}_k$ describes the difference between $\hat{\boldsymbol{z}}_k$ and the actual measurement vector $\boldsymbol{z}_k$. Finally, the UKF provides a-posteriori state and covariance estimates as

$$\begin{aligned} \hat{\boldsymbol{p}}_k &= \hat{\boldsymbol{p}}_k^- + \boldsymbol{K}_k \hat{\boldsymbol{y}}_k \\ \boldsymbol{P}_k &= \boldsymbol{P}_k^- - \boldsymbol{K}_k \hat{\boldsymbol{P}}_{zz,k} \boldsymbol{K}_k^\mathsf{T}, \end{aligned} \tag{S13}$$

where the measurement residual covariance $\hat{\boldsymbol{P}}_{zz,k}$ is calculated in the same manner as is done for the a-priori state covariance in (S11). Using the estimated cross-covariance between predicted state and predicted measurement $\hat{\boldsymbol{P}}_{pz,k}$, the Kalman gain is [S10]

$$\boldsymbol{K}_k = \hat{\boldsymbol{P}}_{pz,k}\hat{\boldsymbol{P}}_{zz,k}^{-1}. \tag{S14}$$

For $\lambda = \eta_1^2(n_p+\eta_3) - n_p$, most literature suggests small positive values for η_1 (e.g., $10^{-3} \leq \eta_1 \leq 1$) and $\eta_3 = 0$ [S10, S12]. However, choosing such values leads to $\lambda < 0$ and ultimately the weights $W_i^{(m)}$ in (S10) to become negative. As a result, it is not guaranteed anymore that, even though the individual expected measurements $\boldsymbol{\mathcal{Z}}_{i,k}$ for all sigma points are constrained to the intervals $\hat{c}_{i,k} \in [0,1]$ and $\hat{s}_{i,k} \in [-1,1]$, their weighted sum (cf. (S12)) remains within these bounds. This can be ensured, however, with purely positive weights. To achieve that, we set the parameters to $\{\eta_1, \eta_2, \eta_3\} = \{1, 0, 3\}$ as suggested in [S13].

The UKF's task is to estimate the local tissue geometry around the contact point between ultrasound probe and tissue surface. As summarized in O_3 we choose to estimate the local tissue geometry up to second order, i.e., we are interested in the position of the contact point (0th order), the normal vector (1st order) and the curvature tensor (2nd order). In the subsequent sections we specify and develop the required quantities for the UKF filter algorithm (S7), (S8): the state vector $\boldsymbol{p}$, the measurement vector $\boldsymbol{z}$, the process model f, and the measurement model h.

b) State vector: Let $\boldsymbol{\psi} \in \mathcal{S}_u$ be the point of interest where the probe at position $\boldsymbol{x}_t$ touches $\mathcal{S}_u$. Furthermore, let $\boldsymbol{\chi} \in \mathcal{S}_b$ be the corresponding proxy point on the base surface $\mathcal{S}_b$, i.e., the orthogonal projection of $\boldsymbol{x}_t$ onto $\mathcal{S}_b$. The variable $\delta \in \mathbb{R}$ in (S16) describes the signed distance of the actual tissue surface $\mathcal{S}_u$ relative to $\mathcal{S}_b$

$$\delta = \operatorname{sign}\left(\boldsymbol{n}_b(\boldsymbol{\chi}) \cdot (\boldsymbol{\psi} - \boldsymbol{\chi})\right) \|\boldsymbol{\psi} - \boldsymbol{\chi}\|_2, \tag{S15}$$

thus being the (vertical, signed) distance between the contact- $\boldsymbol{\psi}$ and proxy point $\boldsymbol{\chi}$. This is the first of the states estimating the local tissue surface $\mathcal{S}_u$ around $\boldsymbol{\psi}$ (cf. Fig. S11)

$$\boldsymbol{p} = \begin{pmatrix}\delta & \kappa & \theta & \varphi\end{pmatrix}^{\mathsf{T}} \in \mathbb{R}^4. \tag{S16}$$

The second state κ represents the normal curvature of $\mathcal{S}_u$ in the direction of the ultrasound probe scan axis. Let $\boldsymbol{\nu} \in \mathbb{R}^3$ be the unit vector representing that scan axis, i.e., the axis along which the individual sensor elements are arranged for the current β, and consider $\boldsymbol{n}_u(\boldsymbol{\psi})$ the unit normal vector at the contact point, such that $\boldsymbol{n}_u : \mathcal{S}_u \to \mathbb{S}^2$ with the unit-sphere $\mathbb{S}^2$. Then, $\Gamma = \operatorname{span}\{\boldsymbol{\nu}_{||}\,, \boldsymbol{n}_u\}$ describes the plane spanned by $\boldsymbol{\nu}_{||}$, the component of $\boldsymbol{\nu}$ tangent to $\mathcal{S}_u$ at $\boldsymbol{\psi}$, and $\boldsymbol{n}_u$. $\{\boldsymbol{\nu}_{||}, \boldsymbol{n}_u\}$ form an orthonormal basis of Γ and serve as coordinate axes of a local coordinate system $\{\mathsf{L}\}$ with origin at $\boldsymbol{\psi}$ and coordinates (γ_1, γ_2). Using the concepts introduced in Supplementary B-A, in an infinitesimal neighborhood of $\boldsymbol{\psi}$ the planar section of $\mathcal{S}_u$ obtained by intersecting the surface with the plane Γ can be described by, either the osculating circle, or a parabola satisfying (ignoring higher order terms)

$$\gamma_2 = -\frac{1}{2}\kappa\gamma_1^2, \tag{S17}$$

with the normal curvature κ of $\mathcal{S}_u$ in the direction of $\boldsymbol{\nu}$. Lastly, θ and φ are the spherical coordinates (cf. Fig. 7E), more precisely the polar and azimuthal angle, of $\boldsymbol{n}_u(\boldsymbol{\psi})$. To avoid the pole singularity at $\boldsymbol{n}_u = \begin{pmatrix}0 & 0 & 1\end{pmatrix}^{\mathsf{T}}$ (arbitrary φ), we adapt the standard convention of spherical coordinates to have the pole at $\boldsymbol{n}_u = \begin{pmatrix}\pm 1 & 0 & 0\end{pmatrix}^{\mathsf{T}}$. The conversion back to Cartesian coordinates then becomes

$$\boldsymbol{n}_u = \begin{pmatrix}\cos(\theta) \\ \sin(\theta)\cos(\varphi) \\ \sin(\theta)\sin(\varphi)\end{pmatrix}. \tag{S18}$$

By restricting both angles to the range $\theta, \varphi \in (0, \pi)$ we assume the tissue surface $\mathcal{S}_u$ to have normal vectors lying only on the upper hemisphere.

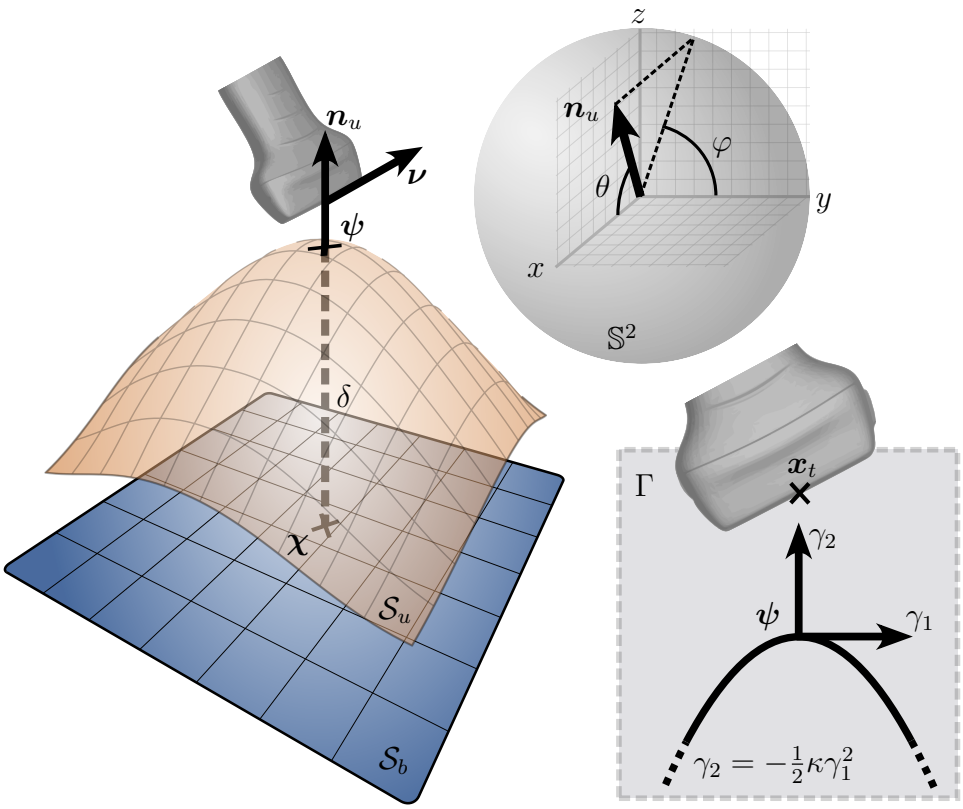

Fig. S11. **UKF state vector.** The state vector comprises the height δ of $\mathcal{S}_u$ relative to $\mathcal{S}_b$ at the contact point, the normal curvature κ of $\mathcal{S}_u$ in the plane Γ, and the spherical coordinates θ, φ of the corresponding unit normal vector.

c) Measurement vector: We choose the measurement

$$\boldsymbol{z} = \begin{pmatrix} c \\ s \end{pmatrix} \in [0,1] \times [-1,1], \tag{S19}$$

with c and s being the coverage and symmetry of acoustic coupling as derived in (3). Fig. S12a visualizes the measurements. The coverage has its maximum $c = 1$ when all scanlines show acoustic coupling, while being zero when the ultrasound probe is nowhere in contact with the tissue. Thus, c is an indication of good image quality. The symmetry s becomes maximal or minimal when acoustic coupling is affecting only one half of the ultrasound image. It therefore provides information about the in-plane orientation of the ultrasound probe, with $s = 0$ indicating good alignment.

d) Process model: Since this work deals with probe landing on a single point on the tissue, it is fair to assume the states $(\delta, \theta, \varphi)$ constant. The normal curvature κ generally changes with ultrasound probe orientation β for the same contact point: for distinct principal curvatures rotating the probe around the surface normal will change the normal curvature. However, we assume no prior knowledge on the curvature tensor and thus have no information on the rate of change $\partial\kappa/\partial\beta$. Hence, we assume κ quasi-stationary and the process model (S7) is simply

$$\hat{\boldsymbol{p}}_k^- = \hat{\boldsymbol{p}}_{k-1} + \boldsymbol{w}_{k-1}. \tag{S20}$$

e) Measurement model: The measurement model provides expected measurements $\hat{\boldsymbol{z}}_k = h(\hat{\boldsymbol{p}}_k^-)$ based on the a-priori state prediction $\hat{\boldsymbol{p}}_k^-$ from (S20). Fig. S12b visualizes the mathematical introduction of the measurement model. The goal is to calculate a w-tuple of binary numbers $\hat{\boldsymbol{a}}_k$ in accordance with (1), (2) that estimates the presence of acoustic coupling given $\hat{\boldsymbol{p}}_k^-$. We omit the time indices for brevity in the following calculations.

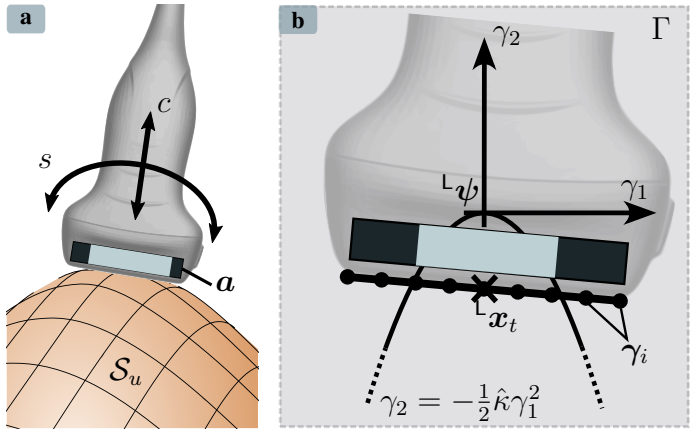

Fig. S12. **UKF measurement vector and model. (a)** The UKF measurements encode information on acoustic shadow in the ultrasound image in two scalar quantities c and s. **(b)** Discretizing the scan axis of the ultrasound probe into $\boldsymbol{\gamma}_i$ points and comparing each to the parabola locally describing $\mathcal{S}_u$ in the plane Γ provides estimated measurements $\hat{\boldsymbol{z}}$.

Express $\boldsymbol{\nu}$ in the local coordinate system $\{\mathsf{L}\}$ by choosing the orthogonal projection of $\boldsymbol{\nu}$ onto the tissue normal $\hat{\boldsymbol{n}}_u$ (their dot product) as γ_2-coordinate and setting the γ_1-coordinate to obtain a unit vector

$$ {}^{\mathsf{L}}\boldsymbol{\nu} = \begin{pmatrix} {}^{\mathsf{L}}\nu_1 \\ {}^{\mathsf{L}}\nu_2 \end{pmatrix} = \begin{pmatrix} \sqrt{1-(\boldsymbol{\nu}^{\mathsf{T}}\hat{\boldsymbol{n}}_u)^2} \\ \boldsymbol{\nu}^{\mathsf{T}}\hat{\boldsymbol{n}}_u \end{pmatrix} \in \mathbb{R}^2. \tag{S21} $$

Set the TCP of the ultrasound probe $\boldsymbol{x}_t$ to be the center of the probe elements at the tip of the probe and express it in local coordinates ${}^{\mathsf{L}}\boldsymbol{x}_t = (0, \hat{d}_u)^{\mathsf{T}}$, with

$$ \hat{d}_u = \begin{pmatrix} 0 & 0 & z_t - \hat{\delta} \end{pmatrix} \hat{\boldsymbol{n}}_u = (z_t - \hat{\delta}) \sin(\hat{\theta}) \sin(\hat{\varphi}) \tag{S22} $$

being the estimated distance to $\mathcal{S}_u$. For a linear ultrasound probe of length l, we calculate w points (w being the width of the ultrasound image $\boldsymbol{\mathcal{I}}_{(w\times h)}$) along the probe axis

$$ \boldsymbol{\gamma}_i = {}^{\mathsf{L}}\boldsymbol{x}_t + \varepsilon_i {}^{\mathsf{L}}\boldsymbol{\nu} \tag{S23} $$

$$ \varepsilon_i = \frac{l(i-1)}{(w-1)} - \frac{l}{2}, \quad i = 1 \dots w. \tag{S24} $$

Then, $\hat{\boldsymbol{a}}$ becomes

$$ \hat{a}_i = \begin{cases} 1 & \text{if } -\frac{1}{2}\hat{\kappa}\gamma_{i,1}^2 > \gamma_{i,2} \\ 0 & \text{otherwise} \end{cases} \quad i = 1 \dots w. \tag{S25} $$

Essentially, for each point $\boldsymbol{\gamma}_i$ along ${}^{\mathsf{L}}\boldsymbol{\nu}$ it is checked whether it lies below or above the surface parabola, with a point being below indicating tissue contact and hence good acoustic coupling along that scanline. Similarly, for a convex probe with curvature κ_p and width l, the measurement model can be derived by replacing (S23) with

$$ \boldsymbol{\gamma}_i = {}^{\mathsf{L}}\boldsymbol{x}_t + \varepsilon_i {}^{\mathsf{L}}\boldsymbol{\nu} + \frac{1}{2}\kappa_p \varepsilon_i^2 {}^{\mathsf{L}}\tilde{\boldsymbol{z}}, \quad i = 1 \dots w, \tag{S26} $$

with ${}^{\mathsf{L}}\tilde{\boldsymbol{z}}$ being the ultrasound probe z-axis expressed in $\{\mathsf{L}\}$. This generalizes to a linear ultrasound probe through $\kappa_p = 0$.

With $\hat{\boldsymbol{a}}$, the expected measurements $\hat{c}$ and $\hat{s}$ are calculated according to (3).

Given the UKF locally describes the planar section of $\mathcal{S}_u$ using a parabola (S17), implementing a rotational trajectory in β essentially results in an osculating paraboloid $\hat{\mathcal{S}}_u$ as a local estimate of $\mathcal{S}_u$ around $\boldsymbol{\psi}$.

D. Acoustic coupling detection

For identifying the probe-tissue contact quality, we perform image processing on the ultrasound images and provide information to the control system for optimization of the contact coupling. The method used in this work is based on [S14], which produces a discrete representation of the tissue within the ultrasound image in form of a sparse point cloud. Through this, it is possible to construct a confidence map of the perceptual quality of the image and detect contact-related acoustic shadow artifacts. The algorithm is capable of detecting acoustic shadow per scanline across the ultrasound image. See Fig. S13 for a visualization of the algorithm described in the following.

Remember the original ultrasound image $\boldsymbol{\mathcal{I}}_{w\times h}$ of width w and height h. For brevity, with a slight abuse of notation we denote $\boldsymbol{\mathcal{I}}_{w\times h} = \boldsymbol{\mathcal{I}}$ in this section. To detect contact-related acoustic shadow, first, areas of dynamic intensity change are detected through iterative Gaussian filtering ($n_f = 5$) following

$$\begin{aligned} \boldsymbol{\mathcal{I}}^{(i)} &= h_f * \boldsymbol{\mathcal{I}}^{(i-1)} \quad i = 1 \dots n_f \\ h_f &= \left(\frac{1}{\sqrt{2\pi\sigma_u}} e^{-u^2/(2\sigma_u^2)}\right)\left(\frac{1}{\sqrt{2\pi\sigma_v}} e^{-v^2/(2\sigma_v^2)}\right), \end{aligned} \tag{S27}$$

with $\boldsymbol{\mathcal{I}}^{(0)} = \boldsymbol{\mathcal{I}}$ and (u, v) the pixel coordinates of each image. The filter parameters are $\sigma_u = 0.2, \sigma_v = 1.8$. Vertical bias of the Gaussian filter, i.e. $\sigma_v \gg \sigma_u$, to be more sensitive to anatomical changes along the vertical direction. Let $\boldsymbol{\mathcal{I}}_{uv} = \boldsymbol{\mathcal{I}}(u, v)$ denote the pixel value of $\boldsymbol{\mathcal{I}}$ at coordinate (u, v). By calculating the per-pixel standard deviation across all filtered images $\boldsymbol{\mathcal{I}}^{(i)}$ (cf. S27)

$$\begin{aligned} \bar{\boldsymbol{\mathcal{I}}}_{uv} = \frac{1}{n_f}\sum_{i=1}^{n_f} \boldsymbol{\mathcal{I}}^{(i)}_{uv}, \;\; S_{uv} = \sqrt{\frac{1}{n_f}\sum_{i=1}^{n_f}\left(\boldsymbol{\mathcal{I}}^{(i)}_{uv} - \bar{\boldsymbol{\mathcal{I}}}_{uv}\right)^2} \\ \boldsymbol{S}_{w\times h} \coloneqq \{S_{uv} \mid (u, v) \in \{1 \dots w\} \times \{1 \dots h\}\}, \end{aligned} \tag{S28}$$

areas of more significant echogenic diversity produce larger intensity outputs. Using a predetermined threshold, a dense 2D point cloud discretizing the ultrasound image is constructed through

$$\Lambda_d \coloneqq \{(u, v) \mid S_{uv} \geq 4\}. \tag{S29}$$

To reduce computation, the point cloud undergoes a sparsification process using an inverse Gaussian density map to determine a set of weights $\boldsymbol{W}_{w\times h}$ of minimum distance for distances to a point.

Using this weight array, the point cloud (S29) is sparsified according to

$$\Lambda_s = \{\lambda_i \in \Lambda_d \mid \forall \lambda_j \in \Lambda_d, j \neq i : \|\lambda_j - \lambda_i\|_2 > W_{\lambda_i}\}. \tag{S30}$$

Here, W_{λ_i} is the weight in $\boldsymbol{W}_{w\times h}$ corresponding to the coordinate of the point $\lambda_i \in \Lambda_d$. Equation (S30) is repeated until all points are separated by their corresponding distances.

Finally, a simplicial complex, i.e., a set of points, edges, triangles, etc., is constructed over the sparsified point cloud (S30). Specifically, due to its simplicity and lack of optimization, a Vietoris–Rips complex is constructed. A Vietoris-Rips complex $\mathcal{VR}(\Lambda_s)$ is a collection of finite subsets of points in Λ_s, such that the pair-wise distance between every element in a subset of $\mathcal{VR}$ is not greater than a given threshold r. Define

$$\mathcal{VR}_n \coloneqq \{\Lambda \subset \mathcal{VR}(\Lambda_s) \mid |\Lambda| = n\} \tag{S31}$$

to be the set of all possible subsets of $\mathcal{VR}(\Lambda_s)$ of size n. Any subset of size n in a Vietoris-Rips complex describes a simplex of order $n - 1$. Consider for example

$$\begin{aligned} \mathcal{VR}_1 &= \{\bullet \subset \mathcal{VR}(\Lambda_s) \mid |\bullet| = 1\} \\ \mathcal{VR}_2 &= \{/ \subset \mathcal{VR}(\Lambda_s) \mid |/| = 2\} \\ \mathcal{VR}_3 &= \{\Delta \subset \mathcal{VR}(\Lambda_s) \mid |\Delta| = 3\} \end{aligned}$$

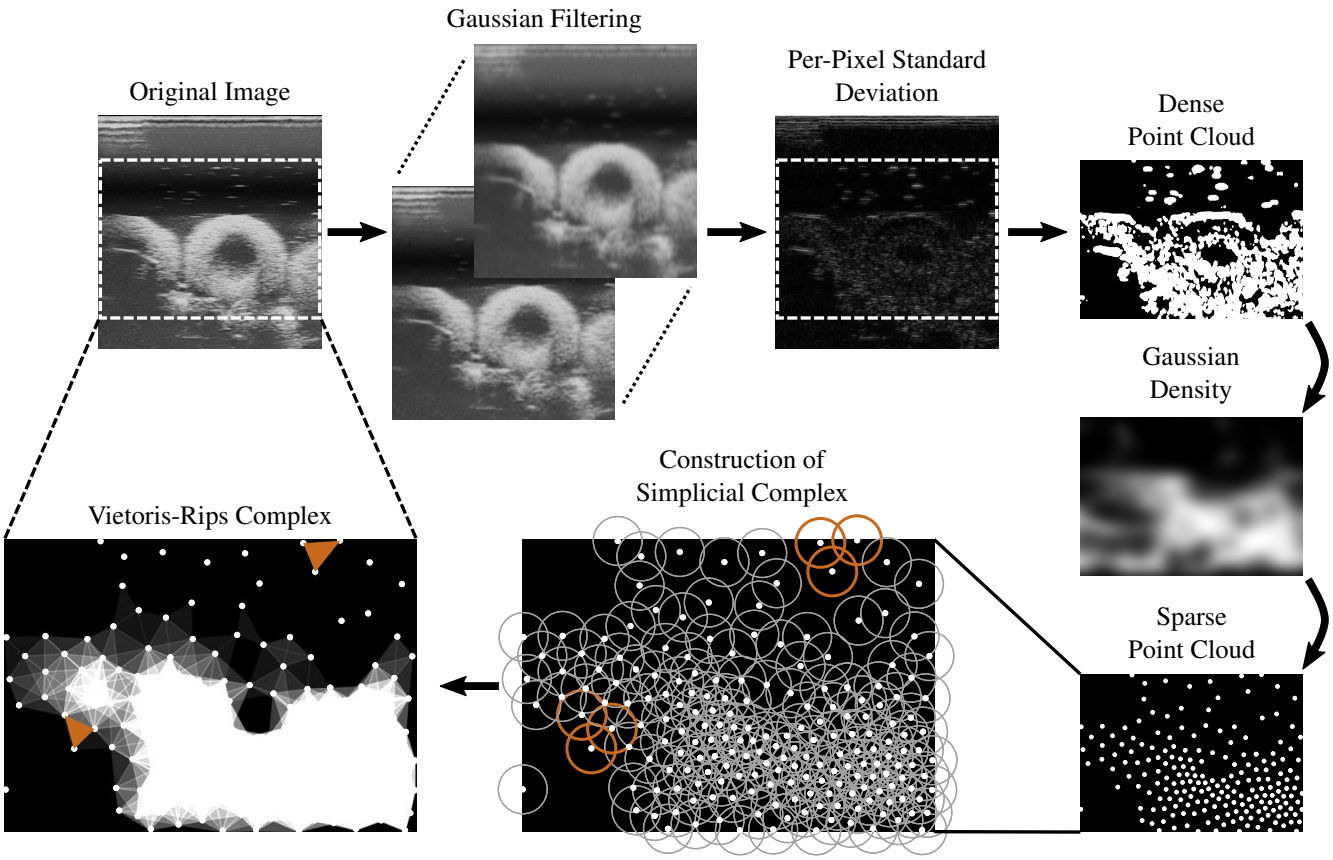

Fig. S13. Ultrasound image quality analysis to identify acoustic shadow. Iterative Gaussian filtering and calculation of per-pixel standard deviation results in a dense point cloud. Sparsification following Gaussian density and construction of a Vietoris-Rips complex leads to a discrete representation of visible tissue within the image. Acoustic shadow is a binary classification based on overlapping triangles along a scanline.

$\mathcal{VR}_1$ describes all 0-simplexes in $\mathcal{VR}$, meaning the points in Λ_s itself. Correspondingly, $\mathcal{VR}_2$ comprises all edges, $\mathcal{VR}_3$ contains all 2-simplexes or triangles. Remember that every subset in $\mathcal{VR}_n$ consists of n elements, and every subset has a diameter at most r.

From this discrete map of the visible tissue in the form of $\mathcal{VR}_3(\Lambda_s)$, acoustic shadow can be classified per scan line as binary w-tuple $\boldsymbol{a} \in \{0,1\}^w$. We define a scan line to be the u-th column of the original image

$$\boldsymbol{\mathcal{I}}_u = \boldsymbol{\mathcal{I}}(u) \coloneqq \{\boldsymbol{\mathcal{I}}_{uv} \subset \boldsymbol{\mathcal{I}} \mid v = 1 \dots h\}. \tag{S32}$$

Acoustic coupling is then classified via analysis of the number of 2D simplexes (triangles) intersecting a scanline

$$a_u = 1 \iff |\{\Delta \in \mathcal{VR}_3 : \Delta \cap \boldsymbol{\mathcal{I}}_u \neq \varnothing\}| \geq 2, \tag{S33}$$

for all scanlines $u = 1 \dots w$. Acoustic coupling, i.e., the absence of acoustic shadow, defined as a classification of 1, is conditional to when this number is above a pre-defined threshold.

E. Servoing Synthesis

The complete ultrasonic servoing control loop is visualized in Fig. S14 and consists of three main sections. The innermost control loop (cf. blue area in Fig. S14) controls the robot manipulator, with torques $\boldsymbol{\tau}$ provided by the surface-centric impedance controller (cf. Supplementary B-B). The UKF, which reads measurements $\boldsymbol{z}$ from the ultrasound probe and approximates the tissue surface locally through the state vector $\hat{\boldsymbol{p}}$, is represented by the orange area in Fig. S14. The local surface estimate $\hat{\mathcal{S}}_u$ is updated after

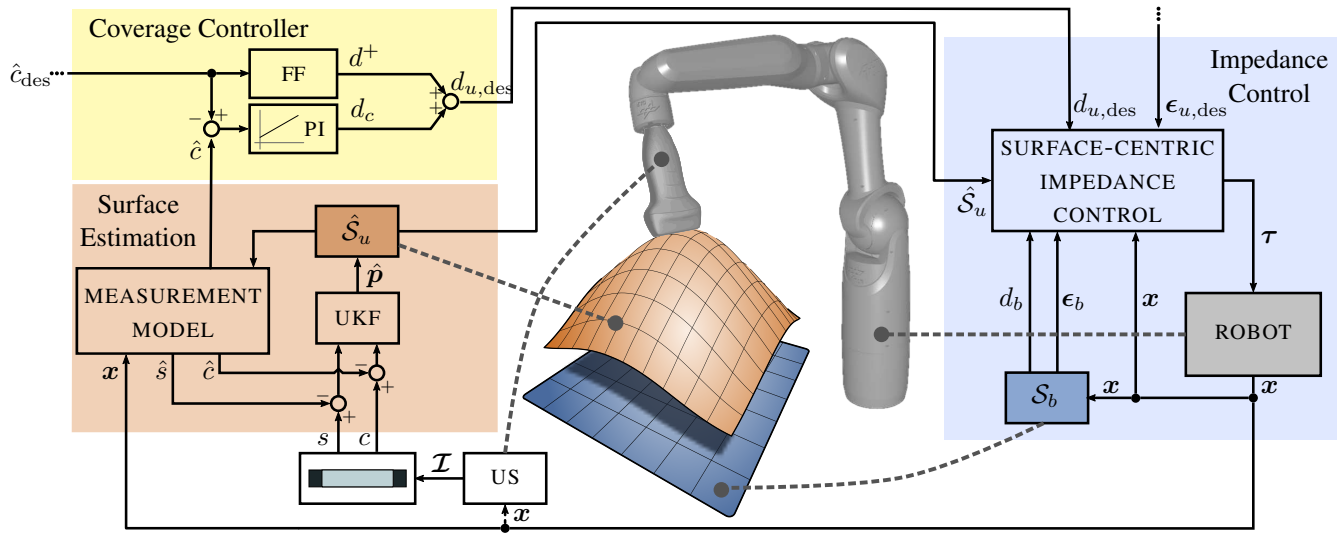

Fig. S14. **Closed loop ultrasonic servoing control.** The surface-centric impedance control provides torques to the robot necessary to establish contact between ultrasound (US) probe and the unknown tissue surface $\mathcal{S}_u$ (blue area). It does so based on the local surface estimate $\hat{\mathcal{S}}_u$ provided by the UKF (orange area). The commanded distance to achieve a desired extent of contact with the tissue is provided by the coverage controller acting on $\hat{c}$ (yellow area).

each filter iteration, which is limited by the frame rate of the ultrasound machine and the rate at which the acoustic coupling tuple (1) is calculated. To smoothen the discrete state updates of the UKF, we add a low-pass filter operating on the estimated states $\hat{\boldsymbol{p}}$ with a cutoff frequency of 1 Hz. Based on $\hat{\mathcal{S}}_u$, the surface-centric impedance control calculates torques necessary to guide the ultrasound probe along the unknown tissue surface $\mathcal{S}_u$. We describe the estimated surface paraboloid $\hat{\mathcal{S}}_u$ in a local coordinate frame $\{\mathsf{S}\}$ with origin $\hat{\boldsymbol{\psi}}$ and axes $\{\hat{\boldsymbol{X}}_{u,1}(\hat{\boldsymbol{\psi}}), \hat{\boldsymbol{X}}_{u,2}(\hat{\boldsymbol{\psi}}), \hat{\boldsymbol{n}}_u(\hat{\boldsymbol{\psi}})\}$ analytically as

$$ {}^{\mathsf{S}}z = -\left(\frac{\hat{\kappa}_1}{2}\,{}^{\mathsf{S}}x^2 + \frac{\hat{\kappa}_2}{2}\,{}^{\mathsf{S}}y^2\right). \tag{S34} $$

We keep track of the maximum and minimum estimated curvature $\hat{\kappa}$ during the UKF operation, to find the principal curvature directions $\hat{\boldsymbol{X}}_{u,1}(\hat{\boldsymbol{\psi}}), \hat{\boldsymbol{X}}_{u,2}(\hat{\boldsymbol{\psi}})$ and their corresponding principal curvature values $\hat{\kappa}_1, \hat{\kappa}_2$. After each filter iteration, $\hat{\mathcal{S}}_u$ is updated to have its vertex at height $\hat{\delta}$, i.e., $\hat{\psi}_z = \hat{\delta}$, and its normal vector at $\hat{\boldsymbol{\psi}}$ aligned with $\hat{\boldsymbol{n}}_u(\hat{\boldsymbol{\psi}})$. With this, we are able to analytically find the proxy point $\hat{\boldsymbol{\chi}}_u \in \hat{\mathcal{S}}_u$, i.e., the point on the estimated paraboloid $\hat{\mathcal{S}}_u$ closest to $\boldsymbol{x}_t$, and the task coordinates in (5) change to

$$ \hat{\boldsymbol{\rho}}_u = \begin{pmatrix} \hat{\boldsymbol{u}}_u(\boldsymbol{q}) \\ \hat{d}_u(\boldsymbol{q}) \\ \hat{\boldsymbol{\epsilon}}_u(\boldsymbol{q}) \end{pmatrix}, \tag{S35} $$

with $\hat{d}_u(\boldsymbol{q}) = (z_t(\boldsymbol{q}) - \hat{\delta})\sin(\hat{\theta})\sin(\hat{\varphi})$ and $\hat{\boldsymbol{\epsilon}}_u(\boldsymbol{q})$ the vector part of the unit quaternion $\hat{\boldsymbol{h}}_u = [\hat{\lambda}_u, \hat{\boldsymbol{\epsilon}}_u]$ describing the orientation of the probe's longitudinal axis relative to the estimated tissue surface normal $\hat{\boldsymbol{n}}_u$. $\hat{\boldsymbol{u}}_u(\boldsymbol{q})$ are parametrization coordinates on $\hat{\boldsymbol{\chi}}_u \in \hat{\mathcal{S}}_u$.

To have the ultrasound probe aligned with the tissue normal, we set $\boldsymbol{\epsilon}_{u,\mathrm{des}} = \boldsymbol{0}$. By assuming the UKF converges to $\hat{\theta} \approx \theta, \hat{\varphi} \approx \varphi$, this is equivalent to realizing a $s = s_{\mathrm{des}} = 0$ for any rotational yaw angle β. As this work deals purely with contact establishment at a static point without moving along the tissue, we specify $\boldsymbol{u}_{u,\mathrm{des}} = \boldsymbol{0}$ to keep the ultrasound probe positioned at $\hat{\boldsymbol{\psi}}$.

a) Coverage controller: We propose setting the desired distance for the surface-centric impedance controller based on a desired coverage c_{des} between ultrasound probe and tissue by implementing a coverage controller (cf. yellow area in Fig. S14). To avoid needing to control the noisy sensor measurement, this desired coupling is specified for the expected measurement $\hat{c}$. Following (S17), the desired distance

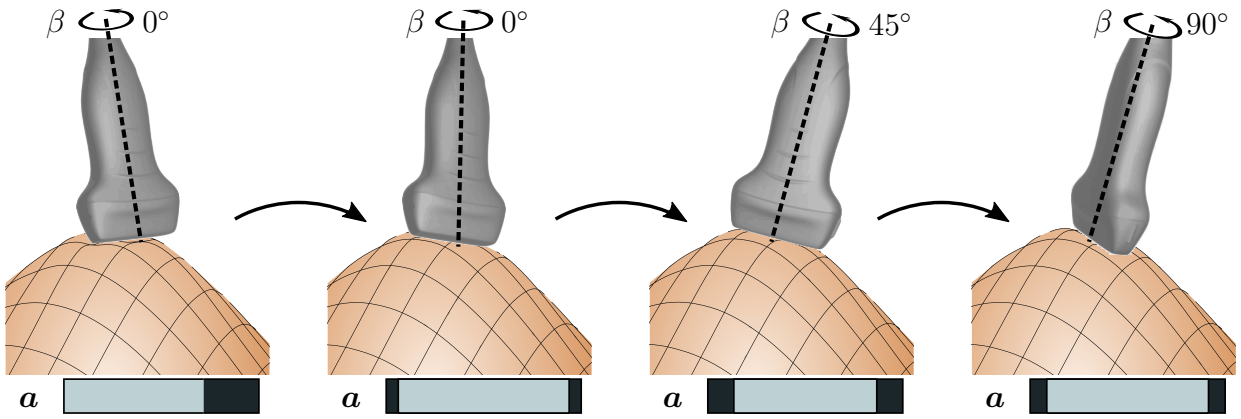

Fig. S15. **The proposed ultrasonic servoing control in action.** Symmetry of the tuple $\boldsymbol{a}$ gives information on the in-plane orientation of the ultrasound probe for a certain yaw angle β. Changing β while keeping $\boldsymbol{a}$ symmetrically distributed ensures the probe is aligned normal to the tissue.

to achieve a certain $\hat{c}_{\text{des}}$ for a linear ultrasound probe of length l, when the probe is aligned normal to the surface is given by the feedforward term

$$d^+ = -\frac{1}{2}\kappa\left(\frac{l}{2}\hat{c}_{\text{des}}\right)^2 = -\frac{l^2}{8}\kappa\hat{c}_{\text{des}}^2. \tag{S36}$$

We use the same feedforward term for a convex ultrasound probe, which is a sufficiently good approximation for small κ_p.

However, by setting $d_{\text{des}} = d^+$ it is not guaranteed that the ultrasound probe actually reaches a $d = d_{\text{des}}$, but rather settles at a distance where the passive interaction forces from controller and object stiffnesses equalize. Hence, we implement an additional PI controller to provide a correction term on the desired distance

$$d_c = k_p e_k + k_i \sum_{j=0}^{k} e_j, \tag{S37}$$

with $e_k = \hat{c}_{\text{des}} - \hat{c}_k$ at time t_k. With that the desired distance of the ultrasound probe becomes $d_{\text{des}} = d^+ + d_c$. The integrator in (S37) ensures that the robot is commanded a distance that results in a convergence to $d = d^+$, where $\hat{c} = c = \hat{c}_{\text{des}}$. To ensure safety, the PI controller (S37) saturates at $d_c = \pm 0.01$ m.

The robot guiding the ultrasound probe can be initialized arbitrarily above the target tissue. As initial state estimates at time $t = t_0$ we set $\hat{\delta}_0 = d_{b,0} + d^+ = z_{t,0} + d^+$, i.e., $\hat{\delta}$ is initialized such that $\hat{c}_0 = \hat{c}_{\text{des}}$ at the initial position $\boldsymbol{x}_{t,0}$ of the ultrasound probe. Correspondingly, $\hat{\boldsymbol{\psi}}_0 = \begin{pmatrix} x_{t,0} & y_{t,0} & \hat{\delta}_0 \end{pmatrix}^\mathsf{T}$. Furthermore, the initial values for $\hat{\theta}_0, \hat{\varphi}_0$ are such that $\hat{\boldsymbol{n}}_{u,0}$ is aligned with the initial z-axis $\tilde{\boldsymbol{z}}_0$ of the ultrasound probe. Lastly, we specify $\hat{\kappa}_0 = 1$, assuming the target tissue to have convex curvature. The yaw angle β is initialized such that $\boldsymbol{\nu}_0$ corresponds to $\beta_0 = 0°$.

When establishing contact, the ultrasonic servoing impedance controller orients the probe to achieve in-plane perpendicularity, i.e., $s \approx 0$, and adjusts the penetration depth to realize a $c \approx \hat{c} \approx \hat{c}_{\text{des}}$. Rotation of the ultrasound probe (cf. Fig. S15 and objective $O_{2.2}$) initiates automatically when the UKF converged in the initial plane Γ_0, as soon as $\hat{\boldsymbol{y}}_k \approx \boldsymbol{0}$.

SUPPLEMENTARY REFERENCES

[S1] U. Seibold, B. Kübler, T. Bahls, R. Haslinger, and F. Steidle, "The dlr mirosurge surgical robotic demonstrator," in *The Encyclopedia of Medical Robotics*. World Scientific, 2019, ch. Chapter 5, pp. 111–142.

[S2] H. Morehouse, H. P. Thaker, and C. Persaud, "Addition of metamucil to gelatin for a realistic breast biopsy phantom," *Journal of ultrasound in medicine*, vol. 26, no. 8, pp. 1123–1126, 2007.

[S3] M. A. Branch, T. F. Coleman, and Y. Li, "A subspace, interior, and conjugate gradient method for large-scale bound-constrained minimization problems," *SIAM Journal on Scientific Computing*, vol. 21, no. 1, pp. 1–23, 1999.

[S4] A. Jacobson, D. Panozzo, et al., *libigl: A simple C++ geometry processing library*, https://libigl.github.io/, 2018.

[S5] T. Needham, *Visual differential geometry and forms: A mathematical drama in five acts*. Princeton: Princeton University Press, 2021.

[S6] M. Dyck, A. Sachtler, J. Klodmann, and A. Albu-Schäffer, "Impedance control on arbitrary surfaces for ultrasound scanning using discrete differential geometry," *IEEE Robotics and Automation Letters*, vol. 7, no. 3, pp. 7738–7746, 2022.

[S7] N. Hogan, "Impedance control: An approach to manipulation," in *1984 American Control Conference*, 1984, pp. 304–313.

[S8] O. Khatib, "A unified approach for motion and force control of robot manipulators: The operational space formulation," *IEEE Journal on Robotics and Automation*, vol. 3, no. 1, pp. 43–53, 1987.

[S9] A. Albu-Schäffer, C. Ott, U. Frese, and G. Hirzinger, "Cartesian impedance control of redundant robots: Recent results with the DLR-light-weight-arms," in *2003 IEEE International conference on robotics and automation*, IEEE, vol. 3, 2003, pp. 3704–3709.

[S10] E. Wan and R. Van Der Merwe, "The unscented kalman filter for nonlinear estimation," in *Proceedings of the IEEE 2000 Adaptive Systems for Signal Processing, Communications, and Control Symposium (Cat. No.00EX373)*, 2000, pp. 153–158.

[S11] S. J. Julier and J. K. Uhlmann, "New extension of the kalman filter to nonlinear systems," in *Signal processing, sensor fusion, and target recognition VI*, Spie, vol. 3068, 1997, pp. 182–193.

[S12] R. Van der Merwe and E. Wan, "The square-root unscented kalman filter for state and parameter-estimation," in *2001 IEEE International Conference on Acoustics, Speech, and Signal Processing. Proceedings (Cat. No.01CH37221)*, vol. 6, 2001, pp. 3461–3464.

[S13] R. D. Turner, "Gaussian processes for state space models and change point detection," Ph.D. dissertation, Apollo - University of Cambridge Repository, Cambridge, UK, 2012.

[S14] A. Weld et al., "Identifying visible tissue in intraoperative ultrasound: A method and application," *International Journal of Computer Assisted Radiology and Surgery*, vol. 20, no. 10, pp. 2107–2117, 2025.

Supplementary Files

This is a list of supplementary files associated with this preprint. Click to download.

- MovieE1.mp4
- DataE1.xlsx
- supplementary.pdf